Turbulent Chemical Non-Equilibrium Reentry Flows in 3D –Five Species

Edisson Sávio de Góes Maciel[1], Cláudia Regina de Andrade[2]

[1]Instituto Tecnológico de Aeronáutica (ITA) – Rua Santa Clara, 245 – Caixa Postal: 2029 – 12.243-970 – São José dos Campos – SP – Brazil
[2]Instituto Tecnológico de Aeronáutica (ITA) – Praça Mal. do Ar Eduardo Gomes, 50 – 12.228-900 – São José dos Campos – SP – Brazil

Abstract In this work, the Favre-averaged Navier-Stokes equations, in conservative and finite volume contexts, employing structured spatial discretization, are studied. Turbulence is taken into account considering the implementation of five k-ω two-equation turbulence models, based on the works of Coakley 1983; Wilcox; Yoder, Georgiadids and Orkwis; Coakley 1997; and Rumsey, Gatski, Ying and Bertelrud. The numerical experiments are performed using the Van Leer numerical algorithm. TVD high resolution is obtained by the use of a MUSCL procedure. Chemical non-equilibrium is studied using a five species chemical model. The results have indicated that the Rumsey, Gatski, Ying and Bertelrud non-linear turbulence model yields the best prediction of the stagnation pressure value, although the Coakley 1983 turbulence model is more computationally efficient.

Keywords k-ω two-equation models, Van Leer scheme, Reentry flows, Favre-averaged Navier-Stokes equations, Chemical non-equilibrium, Five species chemical model

1. Introduction

Renewed interest in the area of hypersonic flight has brought computational fluid dynamics (CFD) to the forefront of fluid flow research [1]. Many years have seen a quantum leap in advancements made in the areas of computer systems and software which utilize them for problem solving. Sophisticated and accurate numerical algorithms are devised routinely that are capable of handling complex computational problems. Experimental test facilities capable of addressing complicated high-speed flow problems are still scarce because they are too expensive to build and sophisticated measurements techniques appropriate for such problems, such as the non-intrusive laser, are still in the development stage. As a result, CFD has become a vital tool, in some cases the only tool, in the flow research today.

In high speed flows, any adjustment of chemical composition or thermodynamic equilibrium to a change in local environment requires certain time. This is because the redistribution of chemical species and internal energies require certain number of molecular collisions, and hence a certain characteristic time. Chemical non-equilibrium occurs when the characteristic time for the chemical reactions to reach local equilibrium is of the same order as the characteristic time of the fluid flow. Similarly, thermal non-equilibrium occurs when the characteristic time for translation and various internal energy modes to reach local equilibrium is of the same order as the characteristic time of the fluid flow. Since chemical and thermal changes are the results of collisions between the constituent particles, non-equilibrium effects prevail in high-speed flows in low-density air.

In chemical non-equilibrium flows the mass conservation equation is applied to each of the constituent species in the gas mixture. Therefore, the overall mass conservation equation is replaced by as many species conservation equations as the number of chemical species considered. The assumption of thermal non-

equilibrium introduces additional energy conservation equations – one for every additional energy mode. Thus, the number of governing equations for non-equilibrium flow is much bigger compared to those for perfect gas flow. A complete set of governing equations for non-equilibrium flow may be found in [2-3].

In spite of the advances made in the area of compressible turbulence modeling in recent years, no universal turbulence model, applicable to such complex flow problems has emerged so far. While the model should be accurate it should also be economical to use in conjunction with the governing equations of the fluid flow. Taking these issues into consideration, k-ω two-equation models have been chosen in the present work [4-8]. These models solve differential equations for the turbulent kinetic energy and the vorticity. Additional differential equations for the variances of temperature and species mass fractions have also been included. These variances have been used to model the turbulence-chemistry interactions in the reacting flows studied here.

Second order spatial accuracy can be achieved by introducing more upwind points or cells in the schemes. It has been noted that the projection stage, whereby the solution is projected in each cell face (i-1/2,j,k; i+1/2,j,k) on piecewise constant states, is the cause of the first order space accuracy of the Godunov schemes ([9]). Hence, it is sufficient to modify the first projection stage without modifying the Riemann solver, in order to generate higher spatial approximations. The state variables at the interfaces are thereby obtained from an extrapolation between neighboring cell averages. This method for the generation of second order upwind schemes based on variable extrapolation is often referred to in the literature as the MUSCL approach. The use of nonlinear limiters in such procedure, with the intention of restricting the amplitude of the gradients appearing in the solution, avoiding thus the formation of new extrema, allows that first order upwind schemes be transformed in TVD high resolution schemes with the appropriate definition of such nonlinear limiters, assuring monotone preserving and total variation diminishing methods.

In the current work, the Favre-averaged Navier-Stokes equations are studied, employing structured spatial discretization, with a conservative and finite volume approaches. Turbulence is taken into account considering the implementation of five k-ω two-equation turbulence models, based on the works of [4-8]. The numerical algorithm of [10] is used to perform the reentry flow numerical experiments, which give us an original contribution to the CFD community. TVD high resolution is obtained by the use of a MUSCL procedure. Two methods of time marching are evaluated to verify their potentialities, namely: Middle Point and Euler Modified. The "hot gas" hypersonic flow around a blunt body, in three-dimensions, is simulated. The convergence process is accelerated to steady state condition through a spatially variable time step procedure, which has proved effective gains in terms of computational acceleration ([11-12]). The reactive simulations involve Earth atmosphere chemical model of five species and seventeen reactions, based on the [13] model. N, O, N_2, O_2, and NO species are used to perform the numerical comparisons. The results have indicated that the [8] turbulence model yields the best prediction of the stagnation pressure value, although the [4] turbulence model is more computationally efficient.

2. Favre Average
The Navier-Stokes equations and the equations for energy and species continuity which governs the flows with multiple species undergoing chemical reactions have been used [14, 15, 16] for the analysis. Details of the present implementation for the five species chemical model, and the specification of the thermodynamic and transport properties are described in [17-18]. Density-weighted averaging [19] is used to derive the turbulent flow equations from the above relations. For a detailed description of the Favre equations, the g's equations and the modeling are presented in [20]. The interested reader is encouraged to read this paper.

3. Navier-Stokes Equations
The flow is modeled by the Favre-averaged Navier-Stokes equations in the condition of chemical non-equilibrium. Details of the five species model implementation are described in [17-18], and the interested reader is encouraged to read these works to become aware of the present study.

The reactive Navier-Stokes equations in chemical non-equilibrium were implemented on conservative and finite volume contexts, in the three-dimensional space. In this case, these equations in integral and conservative forms can be expressed by:

$$\frac{\partial}{\partial t}\int_V Q dV + \int_S \vec{F}\bullet\vec{n}dS = \int_V S_{CV}dV + \int_V T dV, \text{ with}$$

$$\vec{F}=\left(E_e - E_v\right)\vec{i} +\left(F_e - F_v\right)\vec{j} +\left(G_e - G_v\right)\vec{k}, \tag{1}$$

where: Q is the vector of conserved variables, V is the volume of a computational cell, $\vec{F}$ is the complete flux vector, $\vec{n}$ is the unity vector normal to the flux face, S is the flux area, T is the k-ω two-equation model source term, S_C is the chemical source term, E_e, F_e, and G_e are the convective flux vectors or the Euler flux vectors in the x, y, and z directions, respectively, E_v, F_v, and G_v are the viscous flux vectors in the x, y, and z directions, respectively. The $\vec{i}$, $\vec{j}$, and $\vec{k}$ unity vectors define the Cartesian coordinate system. Thirteen (13) conservation equations are solved: one of general mass conservation, three of linear momentum conservation, one of total energy, four of species mass conservation, two of the k-ω turbulence model, and two of the g-equations. Therefore, one of the species is absent of the iterative process. The CFD literature recommends that the species of biggest mass fraction of the gaseous mixture should be omitted, aiming to result in a minor numerical accumulation error, corresponding to the biggest mixture constituent (in the case, the air). To the present study, in which is chosen a chemical model to the air composed of five (5) chemical species (N, O, N_2, O_2 and NO) and seventeen (17) chemical reactions, being fifteen (15) dissociation reactions (endothermic reactions) and two (2) of exchange or recombination, this species can be the N_2 or the O_2. To this work, it was chosen the N_2. The vectors Q, E_e, F_e, G_e, E_v, F_v, G_v, S_C and T can, hence, be defined as follows:

$$Q=\left\{\begin{array}{c}\rho\\\rho u\\\rho v\\\rho w\\ e\\\rho_1\\\rho_2\\\rho_4\\\rho_5\\\rho k\\\rho\omega\\\rho Q_h\\\rho Q_s\end{array}\right\}, E_e=\left\{\begin{array}{c}\rho u\\\rho u^2+p\\\rho uv\\\rho uw\\\rho Hu\\\rho_1 u\\\rho_2 u\\\rho_4 u\\\rho_5 u\\\rho ku\\\rho\omega u\\\rho Q_h u\\\rho Q_s u\end{array}\right\}, F_e=\left\{\begin{array}{c}\rho v\\\rho vu\\\rho v^2+p\\\rho vw\\\rho Hv\\\rho_1 v\\\rho_2 v\\\rho_4 v\\\rho_5 v\\\rho kv\\\rho\omega v\\\rho Q_h v\\\rho Q_s v\end{array}\right\}, G_e=\left\{\begin{array}{c}\rho w\\\rho wu\\\rho wv\\\rho w^2+p\\\rho Hw\\\rho_1 w\\\rho_2 w\\\rho_4 w\\\rho_5 w\\\rho kw\\\rho\omega w\\\rho Q_h w\\\rho Q_s w\end{array}\right\}, E_v=\frac{1}{Re}\left\{\begin{array}{c}0\\ t_{xx}+\tau_{xx}\\ t_{xy}+\tau_{xy}\\ t_{xz}+\tau_{xz}\\ f_x-\phi_x\\-\rho_1 v_{1x}-\theta_{1x}\\-\rho_2 v_{2x}-\theta_{2x}\\-\rho_4 v_{4x}-\theta_{4x}\\-\rho_5 v_{5x}-\theta_{5x}\\\alpha_x\\\beta_x\\\gamma_x\\\delta_x\end{array}\right\}; \tag{2}$$

in which: ρ is the mixture density; u, v, and w are Cartesian components of the velocity vector in the x, y, and z directions, respectively; p is the fluid static pressure; e is the fluid total energy; ρ_1, ρ_2, ρ_4 and ρ_5 are densities of the N, O, O_2 and NO, respectively; k is the turbulent kinetic energy; ω is the turbulent vorticity; Q_h is the product of fluctuating enthalpy, $\overline{h''h''}$; Q_s is the sum of the product of fluctuating mass fraction, $\sum_{i=1}^{ns}\overline{c_i''c_i''}$; H is the mixture total enthalpy; the τ's are the components of the Reynolds stress tensor; the t's are the components of the viscous stress tensor; f_x,f_y, and f_z are viscous work and Fourier heat flux functions; $\rho_s v_{sx}$, $\rho_s v_{sy}$, and $\rho_s v_{sz}$ represent the species diffusion flux, defined by the Fick law; ϕ_x, ϕ_y, and ϕ_z are the terms of mixture diffusion; α_x, α_y, α_z, β_x, β_y, β_z, γ_x, γ_y, γ_z, δ_x, δ_y, and $\delta_z$are two-equation turbulence model parameters; θ_{sx}, θ_{sy}, and θ_{sz} are

diffusion terms function of the mass fraction gradients; $\dot{\omega}_s$ is the chemical source term of each species equation, defined by the law of mass action; T_k and T_ω are k-ω source terms; μ_T is the turbulent viscosity or vorticity viscosity; Prd_T is the turbulent Prandtl number; Sc_T is the turbulent Schmidt number; h is the static enthalpy; and c_T is the total mass fraction sum.

$$F_v = \frac{1}{Re}\begin{Bmatrix} 0 \\ t_{xy} + \tau_{xy} \\ t_{yy} + \tau_{yy} \\ t_{yz} + \tau_{yz} \\ f_y - \phi_y \\ -\rho_1 v_{1y} - \theta_{1y} \\ -\rho_2 v_{2y} - \theta_{2y} \\ -\rho_4 v_{4y} - \theta_{4y} \\ -\rho_5 v_{5y} - \theta_{5y} \\ \alpha_y \\ \beta_y \\ \gamma_y \\ \delta_y \end{Bmatrix} \text{ and } G_v = \frac{1}{Re}\begin{Bmatrix} 0 \\ t_{xz} + \tau_{xz} \\ t_{yz} + \tau_{yz} \\ t_{zz} + \tau_{zz} \\ f_z - \phi_z \\ -\rho_1 v_{1z} - \theta_{1z} \\ -\rho_2 v_{2z} - \theta_{2z} \\ -\rho_4 v_{4z} - \theta_{4z} \\ -\rho_5 v_{5z} - \theta_{5z} \\ \alpha_z \\ \beta_z \\ \gamma_z \\ \delta_z \end{Bmatrix}; \tag{3}$$

$$T = \begin{Bmatrix} 0 \\ 0 \\ 0 \\ 0 \\ 0 \\ 0 \\ 0 \\ 0 \\ 0 \\ T_k \\ T_\omega \\ \left(\dfrac{2\mu_T}{Re\,Pr\,d_T}\right)\left[\left(\dfrac{\partial h}{\partial x}\right)^2 + \left(\dfrac{\partial h}{\partial y}\right)^2 + \left(\dfrac{\partial h}{\partial z}\right)^2\right] \\ \left(\dfrac{2\mu_T}{Re\,Sc_T}\right)\left[\left(\dfrac{\partial c_T}{\partial x}\right)^2 + \left(\dfrac{\partial c_T}{\partial y}\right)^2 + \left(\dfrac{\partial c_T}{\partial z}\right)^2\right] + \dfrac{\Psi}{Re} \end{Bmatrix}; \tag{4}$$

$$S_{CV} = \{0 \quad 0 \quad 0 \quad 0 \quad 0 \quad \dot{\omega}_1 \quad \dot{\omega}_2 \quad \dot{\omega}_4 \quad \dot{\omega}_5 \quad 0 \quad 0 \quad 0 \quad 0\}^T. \tag{5}$$

The viscous stresses, in N/m^2, are determined, according to a Newtonian fluid model, by:

$$t_{xx} = [2\mu_M \,\partial u/\partial x - 2/3\mu_M(\partial u/\partial x + \partial v/\partial y + \partial w/\partial z)]; \tag{6}$$

$$t_{xy} = \mu_M(\partial u/\partial y + \partial v/\partial x); \tag{7}$$

$$t_{xz} = \mu_M(\partial u/\partial z + \partial w/\partial x); \tag{8}$$

$$t_{yy} = [2\mu_M(\partial v/\partial y) - 2/3\mu_M(\partial u/\partial x + \partial v/\partial y + \partial w/\partial z)]; \tag{9}$$

$$t_{yz} = \mu_M(\partial v/\partial z + \partial w/\partial y); \tag{10}$$

$$t_{zz} = [2\mu_M(\partial w/\partial z) - 2/3\mu_M(\partial u/\partial x + \partial v/\partial y + \partial w/\partial z)], \tag{11}$$

where μ_M is the molecular viscosity. The components of the turbulent stress tensor (Reynolds stress tensor) are described by the following expressions:

$$\tau_{xx} = [2\mu_T \partial u/\partial x - 2/3\mu_T(\partial u/\partial x + \partial v/\partial y + \partial w/\partial z)] - 2/3Re\rho k; \tag{12}$$

$$\tau_{xy} = \mu_T(\partial u/\partial y + \partial v/\partial x); \tag{13}$$

$$\tau_{xz} = \mu_T(\partial u/\partial z + \partial w/\partial x); \tag{14}$$

$$\tau_{yy} = [2\mu_T \partial v/\partial y - 2/3\mu_T(\partial u/\partial x + \partial v/\partial y + \partial w/\partial z)] - 2/3Re\rho k; \tag{15}$$

$$\tau_{yz} = \mu_T(\partial v/\partial z + \partial w/\partial y); \tag{16}$$

$$\tau_{zz} = [2\mu_T \partial w/\partial z - 2/3\mu_T(\partial u/\partial x + \partial v/\partial y + \partial w/\partial z)] - 2/3Re\rho k. \tag{17}$$

Expressions to f_x, f_y, and f_z are given below:

$$f_x = (t_{xx} + \tau_{xx})u + (t_{xy} + \tau_{xy})v + (t_{xz} + \tau_{xz})w + q_x + k_x; \tag{18}$$

$$f_y = (t_{xy} + \tau_{xy})u + (t_{yy} + \tau_{yy})v + (t_{yz} + \tau_{yz})w + q_y + k_y; \tag{19}$$

$$f_z = (t_{xz} + \tau_{xz})u + (t_{yz} + \tau_{yz})v + (t_{zz} + \tau_{zz})w + q_z + k_z; \tag{20}$$

where q_x, q_y, and q_z are the Fourier heat flux components and are given by:

$$q_x = (\mu_M/Prd_L + \mu_T/Prd_T)\partial h/\partial x; \tag{21}$$

$$q_y = (\mu_M/Prd_L + \mu_T/Prd_T)\partial h/\partial y; \tag{22}$$

$$q_z = (\mu_M/Prd_L + \mu_T/Prd_T)\partial h/\partial z. \tag{23}$$

with Prd_L the laminar Prandtl number. The last terms in Eqs. (18)-(20) are k_x, k_y, and k_z and are defined as follows:

$$k_x = \left(\mu_M + \frac{\mu_T}{\sigma_k}\right)\partial k/\partial x, \; k_y = \left(\mu_M + \frac{\mu_T}{\sigma_k}\right)\partial k/\partial y, \; k_z = \left(\mu_M + \frac{\mu_T}{\sigma_k}\right)\partial k/\partial z; \tag{24}$$

The diffusion terms related to the k-ω equations are defined as:

$$\alpha_x = (\mu_M + \mu_T/\sigma_k)\partial k/\partial x, \; \alpha_y = (\mu_M + \mu_T/\sigma_k)\partial k/\partial y, \; \alpha_z = (\mu_M + \mu_T/\sigma_k)\partial k/\partial z; \tag{25}$$

$$\beta_x = (\mu_M + \mu_T/\sigma_\omega)\partial\omega/\partial x, \; \beta_y = (\mu_M + \mu_T/\sigma_\omega)\partial\omega/\partial y, \; \beta_z = (\mu_M + \mu_T/\sigma)\partial\omega/\partial z; \tag{26}$$

$$\gamma_x = (\mu_M/Prd_L + \mu_T/Prd_T)\partial Q_h/\partial x, \; \gamma_y = (\mu_M/Prd_L + \mu_T/Prd_T)\partial Q_h/\partial y,$$

$$\gamma_z = (\mu_M/Prd_L + \mu_T/Prd_T)\partial Q_h/\partial y; \tag{27}$$

$$\delta_x = (\mu_M/Sc + \mu_T/Sc_T)\partial Q_S/\partial x, \; \delta_y = (\mu_M/Sc + \mu_T/Sc_T)\partial Q_S/\partial y,$$

$$\delta_z = (\mu_M/Sc + \mu_T/Sc_T)\partial Q_S/\partial z, \tag{28}$$

With Sc and Sc_T the laminar and turbulent Schmidt numbers, with values 0.22 and 1.0, respectively. The terms of species diffusion, defined by the Fick law, to a condition of chemical non-equilibrium, are determined by ([21]):

Journal of Scientific and Engineering Research

$$\rho_s v_{sx} = -\rho D_s \frac{\partial c_s}{\partial x}, \ \rho_s v_{sy} = -\rho D_s \frac{\partial c_s}{\partial y}, \ \text{and} \ \rho_s v_{sz} = -\rho D_s \frac{\partial c_s}{\partial z},$$

(29)

with "s" referent to a given species, c_s being the molar fraction of the species, defined as:

$$c_s = \frac{\rho_s}{\rho}$$

(30)

and D_s is the species-effective-diffusion coefficient. The diffusion terms ϕ_x, ϕ_y, and ϕ_z which appear in the energy equation are defined by ([13]):

$$\phi_x = \sum_{s=1}^{ns} \rho_s v_{sx} h_s, \ \phi_y = \sum_{s=1}^{ns} \rho_s v_{sy} h_s, \ \phi_z = \sum_{s=1}^{ns} \rho_s v_{sz} h_s,$$

(31)

being h_s the specific enthalpy (sensible) of the chemical species "s". Finally, the θ's terms of Eqs. (2-3) are described as,

$$\theta_{sx} = \left(\mu_M / Sc + \mu_T / Sc_T\right) \partial c_S / \partial x, \ \theta_{sy} = \left(\mu_M / Sc + \mu_T / Sc_T\right) \partial c_S / \partial y,$$

$$\theta_{sz} = \left(\mu_M / Sc + \mu_T / Sc_T\right) \partial c_S / \partial z.$$

(32)

4. Flux Vector Splitting Scheme

Considering the three-dimensional and structured case, the algorithm follows that described in [17-18], but considering the third momentum equation of Navier-Stokes ones. The speed of sound takes into account the turbulent kinetic energy by the following expression:

$$a = \sqrt{\gamma_{mixture} \frac{p}{\rho} - k},$$

(33)

where $\gamma_{mixture}$ is the ratio of mixture specific heats calculated in each interaction. In other words, the mixture c_p is calculated by a weighted average involving the c_p of each species and the mass fraction of each species considered as weight; in the same form, the mixture c_v is calculated. Finally, the mixture γ is defined as the ratio of mixture c_p and mixture c_v calculated as described above.

The system is solved in two parts separately, according to [22]. The first part takes into account the dynamic part, which considers the Navier-Stokes equations plus the turbulence equations, the second one takes into account the chemical part involving the chemical contributions. Hence, the discrete-dynamic-convective flux, which solves the dynamic and turbulent parts, is given by:

$$R_{i+1/2,j,k} = |S|_{i+1/2,j,k} \left\{ \frac{1}{2} M_{i+1/2,j,k} \left[\begin{pmatrix} \rho a \\ \rho a u \\ \rho a v \\ \rho a w \\ \rho a H \\ \rho a k \\ \rho a \omega \\ \rho a Q_h \\ \rho a Q_s \end{pmatrix}_L + \begin{pmatrix} \rho a \\ \rho a u \\ \rho a v \\ \rho a w \\ \rho a H \\ \rho a k \\ \rho a \omega \\ \rho a Q_h \\ \rho a Q_s \end{pmatrix}_R \right] - \frac{1}{2} \phi_{i+1/2,j,k} \left[\begin{pmatrix} \rho a \\ \rho a u \\ \rho a v \\ \rho a w \\ \rho a H \\ \rho a k \\ \rho a \omega \\ \rho a Q_h \\ \rho a Q_s \end{pmatrix}_R - \begin{pmatrix} \rho a \\ \rho a u \\ \rho a v \\ \rho a w \\ \rho a H \\ \rho a k \\ \rho a \omega \\ \rho a Q_h \\ \rho a Q_s \end{pmatrix}_L \right] \right\} + \begin{pmatrix} 0 \\ S_x p \\ S_y p \\ S_z p \\ 0 \\ 0 \\ 0 \\ 0 \\ 0 \end{pmatrix}_{i+1/2,j,k}$$

,

(34)

and the discrete-chemical-convective flux is defined by:

$$R_{i+1/2,j,k} = \left|S\right|_{i+1/2,j,k} \left\{ \frac{1}{2} M_{i+1/2,j,k} \left[\begin{pmatrix} \rho_1 a \\ \rho_2 a \\ \rho_4 a \\ \rho_5 a \end{pmatrix}_L + \begin{pmatrix} \rho_1 a \\ \rho_2 a \\ \rho_4 a \\ \rho_5 a \end{pmatrix}_R \right] - \frac{1}{2} \phi_{i+1/2,j,k} \left[\begin{pmatrix} \rho_1 a \\ \rho_2 a \\ \rho_4 a \\ \rho_5 a \end{pmatrix}_R - \begin{pmatrix} \rho_1 a \\ \rho_2 a \\ \rho_4 a \\ \rho_5 a \end{pmatrix}_L \right] \right\}, \tag{35}$$

The same definitions presented in [17-18] are valid to this algorithm. Two time marching methods are applied to verify their potentialities: Middle Point and Euler Modified. The Middle Point method is a second-order, two-stage Runge-Kutta one, to the two types of complete flux. To the convective dynamic part, this method can be represented in general form by:

$$Q_{i,j,k}^{(0)} = Q_{i,j,k}^{n}$$
$$Q_{i,j,k}^{(m)} = Q_{i,j,k}^{(0)} - \alpha_m \left(\Delta t_{i,j,k} / V_{i,j,k} \right) \times R(Q_{i,j,k}^{(m-1)}), \tag{36}$$
$$Q_{i,j,k}^{n+1} = Q_{i,j,k}^{(m)}$$

to the convective chemical part, it can be represented in general form by:

$$Q_{i,j,k}^{(0)} = Q_{i,j,k}^{n}$$
$$Q_{i,j,k}^{(m)} = Q_{i,j,k}^{(0)} - \alpha_m \Delta t_{i,j,k} \left\{ R(Q_{i,j,k}^{(m-1)}) / V_{i,j,k} - S_C \left(Q_{i,j,k}^{(m-1)} \right) \right\}, \tag{37}$$
$$Q_{i,j,k}^{n+1} = Q_{i,j,k}^{(m)}$$

where the chemical source term S_C is calculated with the translational/rotational temperature and the α values of each stage are: $\alpha_1 = 1/2$ and $\alpha_2 = 1.0$. The Euler Modified is also defined as a two-stage Runge-Kutta method, with $\alpha_1 = \alpha_2 = 1.0$.

The definition of the dissipation term ϕ determines the particular formulation of the convective fluxes. The choice below corresponds to the [10] scheme, according to [23]:

$$\phi_{i+1/2,j,k} = \phi_{i+1/2,j,k}^{VL} = \begin{cases} \left| M_{i+1/2,j,k} \right|, & \text{if } \left| M_{i+1/2,j,k} \right| \geq 1; \\ \left| M_{i+1/2,j,k} \right| + 0.5 (M_R - 1)^2, & \text{if } 0 \leq M_{i+1/2,j,k} < 1; \\ \left| M_{i+1/2,j,k} \right| + 0.5 (M_L + 1)^2, & \text{if } -1 < M_{i+1/2,j,k} \leq 0. \end{cases} \tag{38}$$

This scheme is first-order accurate in space and in time. The high-order spatial accuracy is obtained, in this study, by the MUSCL procedure.

The viscous formulation follows that of [24], which adopts the Green theorem to calculate primitive variable gradients. The viscous vectors are obtained by arithmetical average between cell (i,j,k) and its neighbors. As was done with the convective terms, there is a need to separate the viscous flux in two parts: dynamical viscous flux, and chemical viscous flux. The dynamical part corresponds to the first five equations of the Navier-Stokes ones plus the four equations of the turbulence model, and the chemical part corresponds to the four equations immediately below the energy equation.

5. MUSCL Procedure

Details of the present implementation of the MUSCL procedure, as well the incorporation of TVD properties to the scheme, can be found in [9]. The expressions to calculate the fluxes following a MUSCL procedure and the nonlinear flux limiter definitions, herein employed, which incorporates TVD properties, are defined as follows. The conserved variables at the interface (i+1/2,j,k) can be considered as resulting from a combination of backward and forward extrapolations. To a linear one-sided extrapolation at the interface between the averaged values at the two upstream cells (i,j,k) and (i-1,j,k), one has:

$$Q^L_{i+1/2,j,k} = Q_{i,j,k} + \frac{\varepsilon}{2}\left(Q_{i,j,k} - Q_{i-1,j,k}\right), (i,j,k), \quad \text{and } Q^R_{i+1/2,j,k} = Q_{i+1,j,k} - \frac{\varepsilon}{2}\left(Q_{i+2,j,k} - Q_{i+1,j,k}\right), (i-1,j,k),$$

(39)

leading to a second order fully one-sided scheme. If the first order scheme is defined by the numerical flux

$$F_{i+1/2,j,k} = F\left(Q_{i,j,k}, Q_{i+1,j,k}\right)$$

(40)

the second order space accurate numerical flux is obtained from

$$F^{(2)}_{i+1/2,j,k} = F\left(Q^L_{i+1/2,j,k}, Q^R_{i+1/2,j,k}\right).$$

(41)

Higher order flux vector splitting methods, such as those studied in this work, are obtained from:

$$F^{(2)}_{i+1/2,j,k} = F^+\left(Q^L_{i+1/2,j,k}\right) + F^-\left(Q^R_{i+1/2,j,k}\right).$$

(42)

All second order upwind schemes necessarily involve at least five mesh points or cells.

To reach high order solutions without oscillations around discontinuities, nonlinear limiters are employed, replacing the term ε in Eq. (39) by these limiters evaluated at the left and at the right states of the flux interface. To define such limiters, it is necessary to calculate the ratio of consecutive variations of the conserved variables. These ratios are defined as follows:

$$r^+_{i-1/2,j,k} = \left(Q_{i+1,j,k} - Q_{i,j,k}\right)/\left(Q_{i,j,k} - Q_{i-1,j,k}\right) \text{ and } r^+_{i+1/2,j,k} = \left(Q_{i+2,j,k} - Q_{i+1,j,k}\right)/\left(Q_{i+1,j,k} - Q_{i,j,k}\right),$$

(43)

where the nonlinear limiters at the left and at the right states of the flux interface are defined by $\Psi^L = \Psi\left(r^+_{i-1/2,j,k}\right)$ and $\Psi^R = \Psi\left(1/r^+_{i+1/2,j,k}\right)$. In this work, five options of nonlinear limiters were considered to the numerical experiments. These limiters are defined as follows:

$$\Psi^{VL}_l(r_l) = \frac{r_l + |r_l|}{1 + r_l}, \text{ [25] limiter;}$$

(44)

$$\Psi^{VA}_l(r_l) = \frac{r_l + r_l^2}{1 + r_l^2}, \text{ Van Albada limiter;}$$

(45)

$$\Psi^{MIN}_l(r_l) = \text{signal}_l \text{MAX}\left(0, \text{MIN}\left(|r_l|, \text{signal}_l\right)\right), \text{ minmod limiter;}$$

(46)

$$\Psi^{SB}_l(r_l) = \text{MAX}\left(0, \text{MIN}(2r_l, 1), \text{MIN}(r_l, 2)\right), \text{ "Super Bee" limiter, due to [26];}$$

(47)

$$\Psi^{\beta-L}_l(r_l) = \text{MAX}\left(0, \text{MIN}(\beta r_l, 1), \text{MIN}(r_l, \beta)\right), \beta\text{-limiter,}$$

(48)

with "l" varying from 1 to 13 (three-dimensional space), signal$_l$ being equal to 1.0 if $r_l \geq 0.0$ and -1.0 otherwise, r_l is the ratio of consecutive variations of the *l*th conserved variable and β is a parameter assuming values between 1.0 and 2.0, being 1.5 the value assumed in this work. With the implementation of the numerical flux vectors following this MUSCL procedure, second order spatial accuracy and TVD properties are incorporated in the algorithms.

6. Turbulence Models

Five turbulence models were implemented according to a k-ω and k$^{1/2}$-ω formulations. Two turbulence models due to Coakley were implemented.

6.1. Coakley turbulence model – 1983

The [4] model is a k$^{1/2}$-ω one. The turbulent Reynolds number is defined as

$$R = \sqrt{k}N/\nu_M.$$

(49)

The production term of turbulent kinetic energy is given by

$$P = \left[\left(\frac{\partial u}{\partial y} + \frac{\partial v}{\partial x}\right)\frac{\partial u}{\partial y} + \left(\frac{\partial u}{\partial z} + \frac{\partial w}{\partial x}\right)\frac{\partial w}{\partial x} + \left(\frac{\partial w}{\partial y} + \frac{\partial v}{\partial z}\right)\frac{\partial v}{\partial z}\right]/Re.$$

(50)

The function χ is defined as

$$\chi = \sqrt{C_\mu P / \omega^2} - 1 . \tag{51}$$

The damping function is given by

$$D = \frac{1 - e^{-\alpha R}}{1 + \beta \chi} . \tag{52}$$

The turbulent viscosity is defined by

$$\mu_T = \mathrm{Re} \, C_\mu D \rho k / \omega , \tag{53}$$

with: C_μ a constant to be defined. To the [4] model, the T_k and T_ω terms have the following expressions:

$$T_k = P_k + D_k \text{ and } T_\omega = P_\omega + D_\omega , \tag{54}$$

where:

$$P_k = \left(\frac{0.5 C_\mu D P}{\omega^2} \right) \rho \omega \sqrt{k} / \mathrm{Re} ; \quad D_k = 0.5 \left[-\frac{2}{3} \left(\frac{\partial u}{\partial x} + \frac{\partial v}{\partial y} \right) \Big/ \omega - 1 \right] \rho \omega \sqrt{k} / \mathrm{Re} ; \tag{55}$$

$$P_\omega = \left(C_1 C_\mu P / \omega^2 \right) \rho \omega^2 / \mathrm{Re} ; \quad D_\omega = \left[-\frac{2}{3} C_1 \left(\frac{\partial u}{\partial x} + \frac{\partial v}{\partial y} \right) \Big/ \omega - C_2 \right] \rho \omega^2 / \mathrm{Re} , \tag{56}$$

where $C_1 = 0.405 D + 0.045$. The closure coefficients adopted for the [4] model are: $\sigma_k = 1.0, \sigma_\omega = 1.3$, $C_\mu = 0.09, C_2 = 0.92, \beta = 0.5, \alpha = 0.0065$, $\mathrm{Prd}_L = 0.72, \mathrm{Prd}_T = 0.9$.

6.2. Wilcox turbulence model

The turbulent viscosity is expressed in terms of k and ω as:

$$\mu_T = \mathrm{Re} \, \rho k / \omega . \tag{57}$$

In this model, the quantities σ_k and σ_ω have the values $1/\sigma^*$ and $1/\sigma$, respectively, where σ^* and σ are model constants. To the [5] model, the T_k and T_ω terms have the following expressions:

$$T_k = P_k - D_k \text{ and } T_\omega = P_\omega - D_\omega , \tag{58}$$

where:

$$P_k = \mu_T \left[\left(\frac{\partial u}{\partial y} + \frac{\partial v}{\partial x} \right) \frac{\partial u}{\partial y} + \left(\frac{\partial u}{\partial z} + \frac{\partial w}{\partial x} \right) \frac{\partial w}{\partial x} + \left(\frac{\partial v}{\partial z} + \frac{\partial w}{\partial y} \right) \frac{\partial v}{\partial z} \right] \Big/ \mathrm{Re} ; \quad D_k = \beta^* \rho k \omega / \mathrm{Re} ; \tag{59}$$

$$P_\omega = \left(\frac{\alpha \omega}{k} \right) P_k \text{ and } D_\omega = \beta \rho \omega^2 / \mathrm{Re} , \tag{60}$$

where the closure coefficients adopted for the [5] model are: $\beta^* = 0.09, \beta = 3/40, \sigma^* = 0.5, \sigma = 0.5$, $\alpha = 5/9$, $\mathrm{Prd}_L = 0.72, \mathrm{Prd}_T = 0.9$.

6.3. Yoder, Georgiadids and Orkwis turbulence model

To the [6] model, the turbulent Reynolds number is specified by:

$$\mathrm{Re}_T = \rho k / (\mu_M \omega) . \tag{61}$$

The parameter α^* is given by:

$$\alpha^* = \left(\alpha_0^* + \mathrm{Re}_T / R_k \right) / \left(1 + \mathrm{Re}_T / R_k \right) . \tag{62}$$

The turbulent viscosity is specified by:

$$\mu_T = \mathrm{Re} \, \alpha^* \rho k / \omega . \tag{63}$$

The source term denoted by T in the governing equations contains the production and dissipation terms of k and ω. To the [6] model, the T_k and T_ω terms have the following expressions:

$$T_k = P_k - D_k \text{ and } T_\omega = P_\omega - D_\omega. \tag{64}$$

To define the production and dissipation terms, it is necessary to define firstly some parameters. The turbulent Mach number is defined as:

$$M_T = \sqrt{2k/a^2}. \tag{65}$$

It is also necessary to specify the function F:

$$F = MAX\left(M_T^2 - M_{T,0}^2, 0.0\right). \tag{66}$$

The β^* parameter is given by:

$$\beta^* = 0.09\left[5/18 + \left(Re_T/R_S\right)^4\right]/\left[1 + \left(Re_T/R_S\right)^4\right]. \tag{67}$$

Finally, the production and dissipation terms of Eq. (64) are given by

$$P_k = \tau_{xy}\frac{\partial u}{\partial y} + \tau_{xz}\frac{\partial w}{\partial x} + \tau_{yz}\frac{\partial v}{\partial z} \text{ and } D_k = \beta^*\rho\omega k\left(1 + \xi_k F\right)/Re; \tag{68}$$

$$P_\omega = \alpha\omega/kP_k \text{ and } D_\omega = \rho\omega^2\left(\beta + \beta^*\xi_\omega F\right)/Re, \tag{69}$$

with:

$$\alpha = 5/9\left(\alpha_0 + Re_T/R_\omega\right)\left(1 + Re_T/R_\omega\right)/\alpha^*. \tag{70}$$

The [6] turbulence model adopts the following closure coefficients: $R_s = 8.0, R_k = 6.0$, $R_\omega = 2.7$, $\xi_k = 1.0$, $\xi_\omega = 0.0$, $\beta = 3/40$, $M_{T,0} = 0.0$, $\alpha_0 = 0.1$, $\alpha_0^* = \beta/3$, $\sigma_k = 2.0$ and $\sigma_\omega = 2.0$.

6.4. Coakley turbulence model - 1997

In the [7] turbulence model, the turbulent viscosity is expressed in terms of k and ω as:

$$\mu_T = Re C_\mu \rho k/\omega. \tag{71}$$

In this model, the quantities σ_k and σ_ω have the values $1/\sigma^*$ and $1/\sigma$, respectively, where σ^* and σ are model constants.

The source term denoted by T in the governing equations contains the production and dissipation terms of k and ω. To the [7] model, the T_k and T_ω terms have the following expressions:

$$T_k = P_k + D_k \text{ and } T_\omega = P_\omega + D_\omega. \tag{72}$$

To define the production and dissipation terms, it is necessary to define firstly some parameters. The $S_{i,j}$ gradient is defined as

$$S_{ij} = 0.5\left(\frac{\partial u}{\partial y} + \frac{\partial v}{\partial x}\right) + 0.5\left(\frac{\partial v}{\partial z} + \frac{\partial w}{\partial y}\right) + 0.5\left(\frac{\partial w}{\partial x} + \frac{\partial u}{\partial z}\right). \tag{73}$$

The gradient S is expressed as

$$S = \sqrt{2S_{ij}S_{ij}}. \tag{74}$$

The η parameter is defined as

$$\eta = S/\omega. \tag{75}$$

The divergent and the parameter λ are determined by

$$D = \frac{\partial u}{\partial x} + \frac{\partial v}{\partial y} + \frac{\partial w}{\partial z} \text{ and } \lambda = \frac{D}{\omega}. \tag{76}$$

The coefficient α_k and α_ω are defined by

Journal of Scientific and Engineering Research

$$\alpha_k = \frac{2}{3}\left(1 + C_\mu \lambda\right) \text{ and } \alpha_\omega = \alpha_k. \tag{77}$$

The terms of production and destruction of kinetic energy are defined as

$$P_k = C_\mu \eta^2 \rho\omega k / \text{Re} \text{ and } D_k = -(\alpha_k \lambda + 1)\rho\omega k / \text{Re}. \tag{78}$$

In relation to the terms of production and destruction of vorticity, new terms are defined. The characteristic turbulent length is expressed as

$$l = \sqrt{k}\big/\omega. \tag{79}$$

The coefficients $\theta_{k\omega}$ and θ_ω are defined as

$$\theta_{k\omega} = l^2\left(\frac{\partial k}{\partial x}\frac{\partial \omega}{\partial x} + \frac{\partial k}{\partial y}\frac{\partial \omega}{\partial y} + \frac{\partial k}{\partial z}\frac{\partial \omega}{\partial z}\right)\Big/(k\omega) \tag{80}$$

$$\theta_\omega = l^2\left(\frac{\partial \omega}{\partial x}\frac{\partial \omega}{\partial x} + \frac{\partial \omega}{\partial y}\frac{\partial \omega}{\partial y} + \frac{\partial \omega}{\partial z}\frac{\partial \omega}{\partial z}\right)^2\Big/\omega^2. \tag{81}$$

The turbulent Reynolds number is determined by

$$R_t = \frac{k}{\nu_m \omega}. \tag{82}$$

Some others parameters are defined

$$R = C_\mu R_t / R_o, \ D_\nu = \text{TANH}(R), \ \theta = \frac{\theta_{k\omega} - \theta_\omega}{D_\nu}; \tag{83}$$

$$\Delta\theta = \text{TANH}(|\theta| - \theta), \ f_{ii} = \frac{1}{\rho\sqrt{k\omega}}(dp/dx + dp/dy + dp/dz), \ f_i = f_{ii}^2; \tag{84}$$

$$\Delta f_i = \text{TANH}(\alpha f_i), \ \Delta w = 1 - \Delta\theta\left(1 - D_\nu^4\right); \tag{85}$$

$$C_1 = 0.675(1 - \Delta w) + (0.35 + 0.25\Delta f_i)\Delta w; \tag{86}$$

$$\sigma_w = (C_2 - C_1)\sqrt{C_\mu}\big/\kappa^2, \ dw = 2\sigma_w \Delta w C_\mu \theta_{k\omega}. \tag{87}$$

Finally, the production and destruction terms of vorticity are defined as

$$P_\omega = C_1 C_\mu \eta^2 \rho\omega^2\big/\text{Re} \text{ and } D_\omega = \left(-C_1\alpha_\omega\lambda - C_2 + dw\right)\rho\omega^2\big/\text{Re}. \tag{88}$$

The closure coefficients assume the following values: $C_\mu = 0.09$, $C_2 = 0.833$, $\alpha = 5.0$, $\sigma_k = 1.0$, $\sigma = 0.5$, $\sigma^* = 0.5$, $\kappa = 0.41$, $R_o = 10.0$, $\text{Prd}_L = 0.72$ and $\text{Prd}_T = 0.9$.

6.5. Rumsey, Gatski, Ying and Bertelrud turbulence model

Finally, the k-ω model of [8] is studied. The equilibrium eddy-viscosity term employed in the diffusion terms is given by

$$\mu_T^* = \text{Re}\, c_\mu^* \rho k \big/\omega, \tag{89}$$

where $c_\mu^* = 0.081$. The explicit nonlinear constitutive equation that is used to close the Reynolds-averaged Navier-Stokes equations is given (after regularization)

$$\rho\tau_{ii} = 2\mu_t\left[S_{ii} - \frac{1}{3}\left(S_{ii} + S_{jj} + S_{kk}\right)\right] + \frac{2\mu_t^{'}\alpha_3}{\omega}\left(S_{ii}W_{ij} + S_{ij}W_{jj} - S_{ik}W_{jk} + S_{ij}W_{ii} - S_{jj}W_{ij} + S_{jk}W_{ik} - S_{ik}W_{ik} -\right.$$

$$\left. S_{jk}W_{jk} + S_{kk}W_{kk}\right) - \frac{4\mu_t^{'}\alpha_2}{\omega}\left(S_{ij}S_{ii} + S_{ij}S_{jj} + S_{ik}S_{kk} - \frac{1}{3}S_{ij}S_{ij}\right) - \frac{2}{3}\rho k\,Re \tag{90}$$

and

$$\rho\tau_{ij} = 2\mu_tS_{ij} + \frac{2\mu_t^{'}\alpha_3}{\omega}\left(S_{ii}W_{ij} + S_{ij}W_{jj} - S_{ik}W_{jk} + S_{ij}W_{ii} - S_{jj}W_{ij} + S_{jk}W_{ik} - S_{ik}W_{ik} - S_{jk}W_{jk} + S_{kk}W_{kk}\right) -$$

$$\frac{4\mu_t^{'}\alpha_2}{\omega}\left(S_{ij}S_{ii} + S_{ij}S_{jj}\right), \tag{91}$$

where

$$S_{ij} = \frac{1}{2}\left(\frac{\partial u_i}{\partial x_j} + \frac{\partial u_j}{\partial x_i}\right) \text{ and } W_{ij} = \frac{1}{2}\left(\frac{\partial u_i}{\partial x_j} - \frac{\partial u_j}{\partial x_i}\right) \tag{92}$$

are the mean-rate-of-strain tensor and the mean-vorticity tensor, respectively. The turbulent viscosity μ_T is

$$\mu_T = Re\,c_\mu\rho k/\omega. \tag{93}$$

and

$$c_\mu = \frac{3(1+\eta^2) + 0.2(\eta^6 + \zeta^6)}{3 + \eta^2 + 6\eta^2\zeta^2 + 6\zeta^2 + \eta^6 + \zeta^6}\alpha_1; \tag{94}$$

$$\eta = (\alpha_2/\omega)(S_{ij}S_{ij})^{\frac{1}{2}} \text{ and } \zeta = (\alpha_3/\omega)(W_{ij}W_{ij})^{\frac{1}{2}}, \tag{95}$$

where:

$$\alpha_1 = (4/3-C_2)(g/2); \; \alpha_2 = (2-C_3)(g/2); \; \alpha_3 = (2-C_4)(g/2); \tag{96}$$

$$g = \frac{1}{C_1/2 + C_5 - 1}. \tag{97}$$

The constants that govern the pressure-strain correlation model of [8] are $C_1 = 6.8$, $C_2 = 0.36$, $C_3 = 1.25$, $C_4 = 0.4$ and $C_5 = 1.88$. The $\mu_T^{'}$ terms considered in Eqs. (90-91) are given by

$$\mu_T^{'} = Re\,c_\mu^{'}\rho k/\omega, \tag{98}$$

where

$$c_\mu^{'} = \frac{3(1+\eta^2)}{3 + \eta^2 + 6\eta^2\zeta^2 + 6\zeta^2 + \eta^6 + \zeta^6}\alpha_1. \tag{99}$$

The source term denoted by T in the governing equation contains the production and dissipation terms of k and ω. To the [8] model, the T_k and T_ω terms have the following expressions:

$$T_k = P_k - D_k \text{ and } T_\omega = P_\omega - D_\omega, \tag{100}$$

where:

$$P_k = \rho\left[\tau_{xy}\frac{\partial u}{\partial y} + \tau_{xz}\frac{\partial w}{\partial x} + \tau_{yz}\frac{\partial v}{\partial z}\right], \quad D_k = \rho\omega k/Re \, ; \tag{101}$$

$$P_\omega = \psi\rho\omega\left(\tau_{xy}\frac{\partial u}{\partial y}\right)\Big/k, \quad \text{and } D_\omega = \beta\rho\omega^2/Re \, . \tag{102}$$

The closure coefficients adopted to the [8] model assume the following values: $\beta = 0.83$, $\kappa = 0.41$, $\sigma_k = 1.4$, $\sigma_\omega = 2.2$, $Prd_L = 0.72$, $Prd_T = 0.9$, $\psi = \beta - \left[\kappa^2/\sigma_\omega\sqrt{c_\mu^*}\right]$.

7. Spatially Variable Time Step

The spatially variable time step has proved efficient gains in terms of convergence acceleration, as proved by [11-12]. The total pressure of the gaseous mixture is determined by Dalton law, which indicates that the total pressure of the gas is the sum of the partial pressure of each constituent gas, resulting in:

$$p_s = c_s\rho R_s T \text{ and } p = \sum_{s=1}^{N} p_s \, . \tag{103}$$

The speed of sound to a reactive mixture and considering turbulence modeling can be, hence, determined by Eq. (33). Finally, the spatially variable time step is defined from the CFL definition:

$$\Delta t_{i,j,k} = \frac{CFL\Delta s_{i,j,k}}{\sqrt{u_{i,j,k}^2 + v_{i,j,k}^2 + w_{i,j,k}^2 + a_{i,j,k}}} \, , \tag{104}$$

where $\Delta s_{i,j,k}$ is the characteristic length of each cell (defined between the minimum cell side and the minimum barycenter distance between each cell and its neighbors).

8. Dimensionless, Initial and Boundary Conditions

8.1. Dimensionless

The dimensionless employed to the chemical non-equilibrium case consisted in: R_s is nondimensionalized by a_{char}, where $a_{char} = \sqrt{\gamma p_\infty/\rho_\infty}$; c_v is nondimensionalized by a_{char}; h_s and h_s^0 are nondimensionalized by a_{char}^2 ; T, translational/rotational temperature, is nondimensionalized by a_{char}; ρ_s and ρ are nondimensionalized by ρ_∞; u, v, and w arenondimensionalized by a_{char}; μ_M is nondimensionalized by μ_∞; D, diffusion coefficient, nondimensionalized by $a_{char}^2 dt_{char}$, where dt_{char} is the minimum time step calculated in the computational domain at the first iteration; $\dot\omega$ is nondimensionalized by $\rho_\infty x10^{-3}/dt_{char}$; e and p arenondimensionalized by $\rho_\infty a_{char}^2$.

8.2. Initial Condition

The initial conditions to this problem, for a five species chemical model, are presented in Table 1. L_{REF} is the reference length, equal to L in the present study. The Reynolds number is obtained from data of [27].

Table 1: Initial conditions to the problem of the blunt body

Property	Value
M_∞	8.78
ρ_∞	0.00326 kg/m^3
p_∞	687 Pa
U_∞	4,776 m/s
T_∞	694 K
Altitude	40,000 m
c_N	10^{-9}
c_O	0.07955

c_{O_2}	0.13400
c_{NO}	0.05090
L	2.0 m
Re_∞	2.3885×10^6
k_∞	10^{-6}
ω_∞	$10u/L_{REF}$
Q_h	$10^{-4} h_\infty^2$
Q_s	$10^{-2} \sum_{s=1}^{N} c_{s,\infty}^2$

8.3. Boundary Conditions

The boundary conditions are basically of three types: solid wall, entrance, and exit. These conditions are implemented with the help of ghost cells.

Wall condition: At a solid boundary the non-slip condition is enforced. Therefore, the tangent velocity component of the ghost volume at wall has the same magnitude as the respective velocity component of its real neighbor cell, but opposite signal. In the same way, the normal velocity component of the ghost volume at wall is equal in value, but opposite in signal, to the respective velocity component of its real neighbor cell.

The normal pressure gradient of the fluid at the wall is assumed to be equal to zero in a boundary-layer like condition. The same hypothesis is applied for the normal temperature gradient at the wall, assuming an adiabatic wall.

From the above considerations, density and translational/rotational temperature are extrapolated from the respective values of its real neighbor volume (zero order extrapolation).

With the species mass fractions and with the definition of the internal energy for each gas, it is possible to obtain the mixture internal energy of the ghost volume. The mixture formation enthalpy is extrapolated from the real cell. The mixture total energy to the ghost cell is calculated by:

$$e_g = \rho_g \left[e_{i,g} + h_{mixture,g}^0 + 0.5 \left(u_g^2 + v_g^2 + w_g^2 \right) \right], \tag{105}$$

where "g" reports to "ghost" cell and $e_{i,g}$ is the internal energy of the mixture. To the species density, the non-catalytic condition is imposed, what corresponds to zero order extrapolation from the real cell species densities.

The turbulent kinetic energy and the turbulent vorticity at the ghost volumes are determined by the following expression:

$$\text{All models: } k_{ghost} = 0.0 \text{ and } \omega_{ghost} = \left[\left(38/3 \nu_M \right) / \left(\overline{\beta} d_n^2 \right) \right], \tag{106}$$

where $\overline{\beta}$ assumes the value 3/40 and d_n is the distance of the first cell to the wall. Values to Q_h and Q_s at the boundary are the same as the initial condition.

Entrance condition: It is divided in two flow regimes:

(a) Subsonic flow: Eight properties are specified and one extrapolated in the boundary conditions of the dynamic part of the algorithm. This approach is based on information propagation analysis along characteristic directions in the calculation domain ([28]). In other words, for subsonic flow, eight characteristic propagate information point into the computational domain. Thus eight flow properties must be fixed at the inlet plane. Just one characteristic line allows information to travel upstream. So, one flow variable must be extrapolated from the grid interior to the inlet boundary. The total energy was the extrapolated variable from the real neighbor volumes, for the studied problem. Density and velocity components adopted values of freestream flow. The turbulence kinetic energy and the vorticity are prescribed and receive the following values: $k = 0.01 k_{ff}$ and

$\omega = 10u/L_{REF}$, respectively, where $k_{ff} = 0.5u^2$. Q_h and Q_s are also fixed with the values $10^{-6} h_\infty^2$ and $10^{-3} \sum_{s=1}^{N} c_{s,\infty}^2$,

respectively. To the chemical part, four information propagate upstream because it is assumed that all four

equations are conducted by the eigenvalue "(q_n-a)". In the subsonic flow, all eigenvalues are negative and the information should be extrapolated. Hence, all of them should be extrapolated.

(b) Supersonic flow: In this case no information travels upstream; therefore all variables are fixed with their of freestream values.

Exit condition: It is also divided in two flow regimes:

(a) Subsonic flow: Eight characteristic propagate information outward the computational domain. Hence, the associated variables should be extrapolated from interior information. The characteristic direction associated to the "$(q_{normal}-a)$" velocity should be specified because it points inward to the computational domain ([28]). In this case, the ghost volume total energy is specified from its initial value. Density, velocity components and turbulent variables are extrapolated. To the chemical part, the eigenvalue "(q_n-a)" is again negative and the characteristics are always flowing in to the computational domain. Hence, the four chemical species under study should have their densities fixed by their freestream values.

(b) Supersonic flow: All variables are extrapolated from interior grid cells, as no flow information can make its way upstream. In other words, nothing can be fixed.

9. Physical Problem and Mesh

One physical problem is studied in this work: the blunt body problem. The geometry under study is a blunt body with 1.0 m of nose ratio and parallel rectilinear walls. The far field is located at 20.0 times the nose ratio in relation to the configuration nose.

Figure 1 shows the viscous mesh used to the blunt body problem. This mesh is composed of 22,932 rectangular cells and 26,500 nodes, employing an exponential stretching of 5.0%. This mesh is equivalent in finite differences to a one of 53x50x10 points. A "O" mesh is taken as the base to construct such mesh. No smoothing is used in this mesh generation process, being this one constructed in Cartesian coordinates.

10. Results

Tests were performed in a Core i7 processor of 2.1GHz and 8.0Gbytes of RAM microcomputer, in a Windows 8.0 environment. Three (3) orders of reduction of the maximum residual in the field were considered to obtain a converged solution; however, with the minimum of two and a half (2.5) orders the author considered the solution converged. The residual was defined as the value of the discretized conservation equation. The entrance or attack angle and the longitudinal angle were adopted equal to zero.

10.1. Coakley Results - 1983

Middle Point Method: Figure 2 shows the pressure contours obtained by the [10] scheme, and employing the [4] turbulence model coupled with the Middle Point time marching method. The value of the pressure peak is around 159.00 unities. Good symmetry properties can be observed. The normal shock wave is also well captured by the numerical algorithm.

Figure 3 exhibits the Mach number contours generated by the [10] numerical scheme, and using the [4] turbulence model coupled with the Middle Point time marching method. Good symmetry properties are observed. The subsonic region behind the normal part of the shock wave is well captured.

Figure 4 presents the O_2 mass fraction contours obtained by the [10] numerical scheme, and employing the [4] turbulence model coupled with the Middle Point time marching method. It is also verified good symmetry properties, with a satisfactory O_2 dissociation.

Figure 5 exhibits the turbulent kinetic energy contours under the same previous numerical scheme selection. These contours show really the contours of $k^{1/2}$. Reasonable values of turbulence can be observed.

Euler Modified Method: Figure 6 shows the pressure contours obtained by the [10] scheme, and using the [4] turbulence model coupled with the Euler Modified time marching method. The pressure peak is also 159.00, the same value obtained by the Middle Point method. Good symmetry properties are observed, and the normal shock wave is well captured by the numerical scheme.

Figure 7 presents the Mach number contours generated by the [10] scheme, using the [4] turbulence model coupled with the Euler Modified method. The contours are free of pre-shock oscillations. Moreover, the subsonic region around the body is well captured by the numerical scheme.

Figure 8 exhibits the O_2 mass fraction contours obtained by the [10] algorithm, employing the [4] turbulence model coupled with the Euler Modified method. Results show reasonable dissociation of O_2 and good symmetry characteristics are also observed.

Figure 9 shows the turbulence kinetic energy contours under the same previous numerical scheme selection. Turbulence level is well captured by the numerical scheme.

10.2. Wilcox Results

Middle Point Method: Figure 10 presents the pressure contours generated by the [10] scheme, and using the [5] turbulence model coupled with the Middle Point method. The pressure peak is 158.93 and good symmetry properties are observed. Besides, the shock wave is well captured by the numerical scheme.

Figure 11 exhibits the Mach number contours generated by the [10] scheme, and employing the [5] turbulence model coupled with the Middle Point method. Solution free of pre-shock oscillations can be verified.

Figure 12 shows the O_2 mass fraction contours obtained by the [10] scheme, and using the [5] turbulence model coupled with the Middle Point method. The dissociation of O_2 is satisfactory and good symmetry properties are also observed.

Figure 13 presents the turbulence kinetic energy contours under the same previous numerical scheme selection. Bigger turbulence effects can be observed when compared to the [4] turbulence model results. In qualitative terms, a significant difference is also perceptible. Again, good symmetry properties are verified.

Euler Modified Method: Figure 14 exhibits the pressure contours obtained by the [10] numerical algorithm, and using the [5] turbulence model coupled withthe Euler Modified method. The pressure peak is 158.94. Good symmetry properties are observed.

Figure 15 shows the Mach number contours obtained by the [10] scheme, and employing the [5] turbulence model coupled withthe Euler Modified method. Good symmetry properties and solution free of pre-shock oscillations can be observed.

Figure 16 presents the O_2 mass fraction contours generated by the [10] scheme, and using the [5] turbulence model coupled with the Euler Modified method. Good dissociation of O_2 is observed. Good symmetry characteristics can be also verified.

Figure 17 exhibits the turbulence kinetic energy contours under the same previous numerical scheme selection. Effects of turbulence are more intense in comparison with the [4] turbulence model results. The [5] qualitative results are again different from the [4] qualitative results. Good symmetry properties are also observed.

10.3. Yoder, Georgiadids and Orkwis Results

Middle Point Method: Figure 18 shows the pressure contours obtained by the [10] scheme, and using the [6] turbulence model coupled with the Middle Point method. Some pre-shock oscillations can be highlighted in the solution. The pressure peak is 158.77 unities. Moreover, good symmetry properties can be observed.

Figure 19 exhibits the Mach number contours generated by the [10] scheme, and employing the [6] turbulence model coupled with the Middle Point method. There is not pre-shock oscillations in the solution and the normal shock wave is well captured.

Figure 20 presents the O_2 mass fraction contours generated by the [10] scheme, and using the [6] turbulence model coupled with the Middle Point method. Good dissociation of O_2 and symmetry properties can be also observed.

Figure 21 shows the turbulence kinetic energy contours generated under the same previous numerical scheme selection. Turbulence effects are detectable, although less intense compared to the [5] results.

Euler Modified Method: Figure 22 exhibits the pressure contours obtained by the [10] scheme, and using the [6] turbulence model coupled with the Euler Modified method. The solution is free of pre-shock oscillations. The pressure peak is 158.77, inferior to that obtained when the [4] turbulence model has been used.

Figure 23 shows the Mach number contours obtained by the [10] scheme, and employing the [6] turbulence model coupled with the Euler Modified method. The subsonic region around the body is well captured by the

numerical scheme. Good symmetry properties can also be verified.

Figure 24 presents O_2 mass fraction contours obtained by the [10] scheme, and using the [6] turbulence model coupled with the Euler Modified method. Good O_2dissociation is perceptible in the mass fraction contours.

Figure 25 shows the turbulence kinetic energy contours generated under the same previous numerical scheme selection. Bigger turbulence effects are observed, however, inferior to those verified in the [5] turbulence model. Good symmetry properties can be observed.

10.4. Coakley Results – 1997

Middle Point Method: Figure 26 exhibits the pressure contours obtained by the [10] numerical scheme, using the [7] turbulence model coupled with the Middle Point method. Solution free of pre-shock oscillations are observed with good symmetry properties. The pressure peak is 158.78.

Figure 27 shows the Mach number contours generated by the [10] algorithm, as using the [7] turbulence model coupled with the Middle Point method. The Mach number contours are of good quality, the subsonic region behind the normal shock wave is well captured, and good symmetry properties are observable.

Figure 28 presents the O_2 mass fraction contours obtained by the [10] numerical algorithm, and using the [7] turbulence model coupled with the Middle Point method. Good dissociation of O_2 can be verified.

Figure 29 exhibits the turbulence kinetic energy contours obtained by the [10] scheme under the same previous numerical scheme selection. Good turbulence effects are satisfactorily captured. The turbulence level is bigger than the results provided by the [4] turbulence model, but inferior to those observed in the [5] turbulence model.

Euler Modified Method: Figure 30 presents the pressure contours obtained by the [10] scheme, and using the [7] turbulence model coupled with the Euler Modified method. The solution is free of pre-shock oscillations. The pressure peak is 158.78. Moreover, good symmetry properties are detected.

Figure 31 shows the Mach number contours generated by the [10] scheme, and employing the [7] turbulence model coupled with the Euler Modified method. No pre-shock oscillations can be verified, but good symmetry properties occur.

Figure 32 exhibits the O_2 mass fraction contours obtained by the [10] scheme, and using the [7] turbulence model coupled with the Euler Modified method. Good dissociation of O_2 is observed in relation to its initial value.

Figure 33 shows the turbulence kinetic energy contours obtained under the same previous numerical scheme selection. Good turbulence effects are perceptible, however, inferior to those observed in the [5] turbulence model.

10.5. Rumsey, Gatski, Ying and Bertelrud Results

Middle Point Method: Figure 34 exhibits the pressure contours obtained by the [10] scheme, and using the [8] turbulence model coupled with the Middle Point method. Good symmetry properties can be observed. The pressure peak is 158.82 unities. Besides, the solution is free of pre-shock oscillations.

Figure 35 shows the Mach number contours generated by the [10] scheme, and employing the [8] turbulence model coupled with the Middle Point time marching method. Good symmetry properties are observed, free of pre-shock oscillations.

Figure 36 presents the O_2 mass fraction contours obtained by the [10] scheme, and using the [8] turbulence model coupled with the Middle Point time marching method. Good O_2dissociation can be detected in relation to the initial condition. Good symmetry properties can also be verified.

Figure 37 shows the turbulence kinetic energy contours generated under the same previous numerical scheme selection. Bigger turbulence effects are perceptible in relation to the other models, however, inferior to those observed in the [5] turbulence model results.

*Euler Modified Method:*Figure 38 exhibits the pressure contours obtained by the [10] numerical algorithm, and using the [8] turbulence model coupled with the Euler Modified method. Good symmetry properties can be observed, free of pre-shock oscillations. The pressure peak is 158.82.

Figure 39 presents the Mach number contours obtained by the [10] scheme, and employing the [8] turbulence model coupled with the Euler Modified method. Good symmetry properties are observed. The Mach number contours present homogenous properties, being of good quality.

Figure 40 shows the O_2 mass fraction contours generated by the [10] scheme, and using the [8] turbulence model coupled with the Euler Modifiedtime marching method. Good dissociation of O_2 can be detectable. Besides, good symmetry properties can be observed.

Figure 41 exhibits the turbulence kinetic energy contours obtained under the same previous numerical scheme selection. A significant amount of turbulence can be observed by the turbulence kinetic energy contours, although inferior to that observed in the [5] turbulence model.

10.6. Other Results

Figure 42 shows the –Cp distributions at wall yielded by the turbulence models when the Middle Point time marching method has been employed. As can be seen, all solutions converge to the same profile, and no significant differences exist. Figure 43 presents the –Cp distributions at wall produced by the turbulence models when using the Euler Modified method. Good agreement among the curves can be observed, without meaningful differences. Figure 44 exhibits the translational/rotational temperature profiles obtained by all five turbulence models when using the Middle Point method. The [4] and [8] profiles are less intense than the other profiles; in other words, the [4] and [8] profiles reach temperatures smaller than the others curves. So, it can be pointed out that the [4] and [8] turbulence models are the most conservative in relation to the other models. Figure 45 shows the translational/rotational temperature profiles obtained by the turbulence models when using de Euler Modified method. The [4] and [8] profiles are again more conservative than the other models, reaching smaller values at wall.

10.7. Quantitative Analysis

In order to perform a quantitative analysis, the present reactive results are compared to the perfect gas solutions. The stagnation pressure at the blunt body nose was evaluated assuming the perfect gas formulation. Such parameter calculated at this way is not the best comparison, but in the absence of practical reactive results, this constitutes the best available solution.
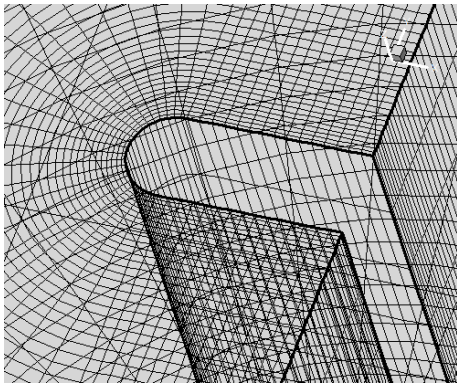
Figure 1: Mesh to blunt body experiments
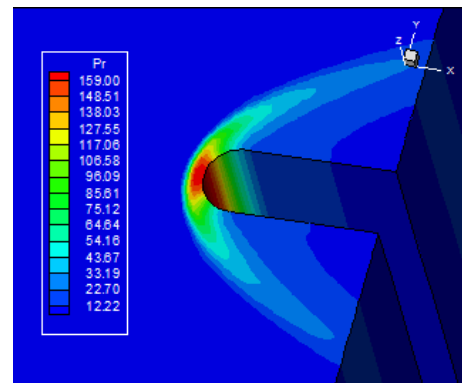
Figure 2: Pressure contours (C83/MP)
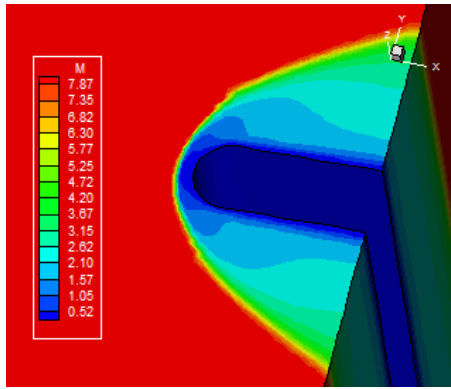
Figure 3: Mach number contours (C83/MP)
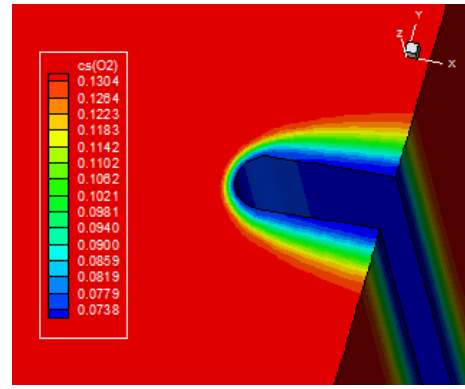

Figure 4: O₂ mass fraction contours (C83/MP)
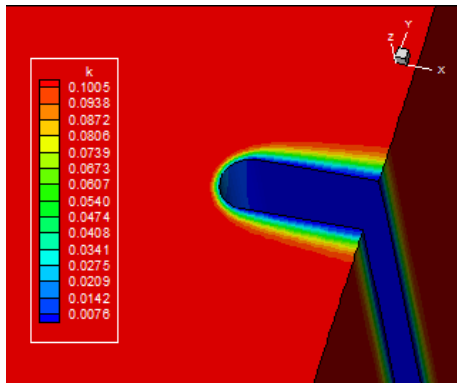
Figure 5: Turbulent kinetic energy contours (C83/MP)
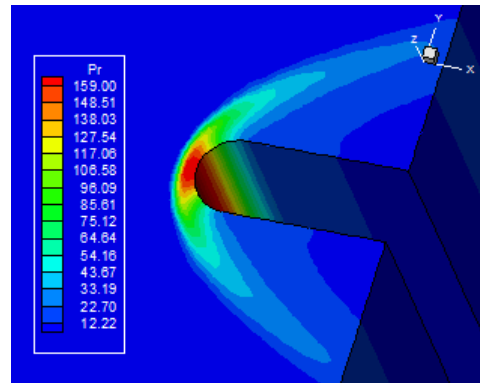

*Figure 6: Pressure contours (C83/EM)*
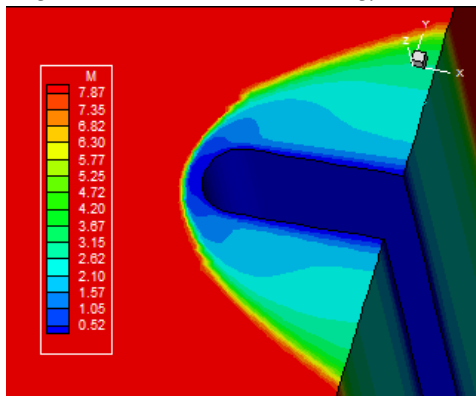

Figure 7: Mach number contours (C83/EM)
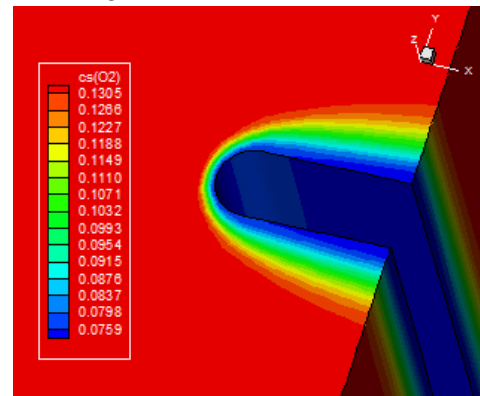
Figure 8: O₂ mass fraction contours (C83/EM)
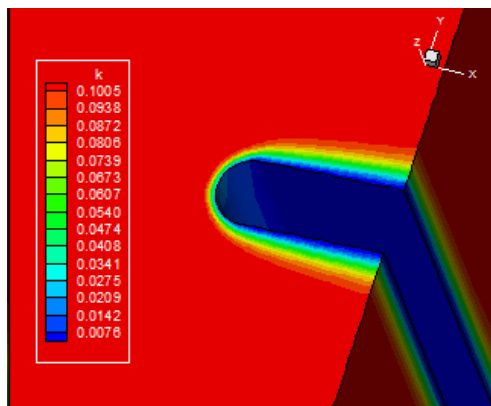
*Figure 9: Turbulent kinetic energy contours (C83/EM)*
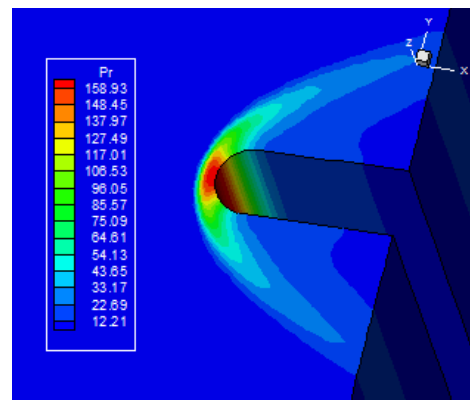
Figure 10: Pressure contours (W88/MP)
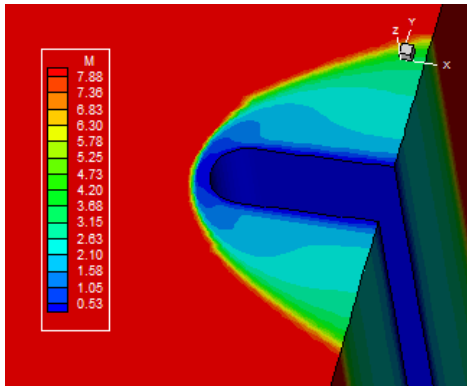
Figure 11: Mach number contours (W88/MP)
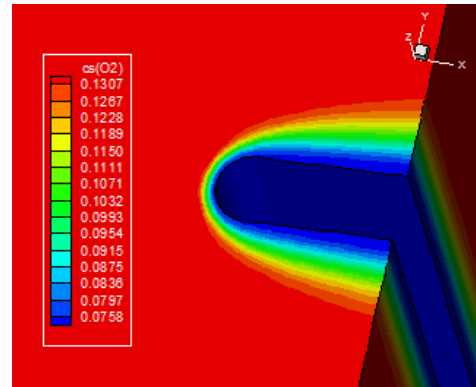
Figure 12: O_2 mass fraction contours (W88/MP)
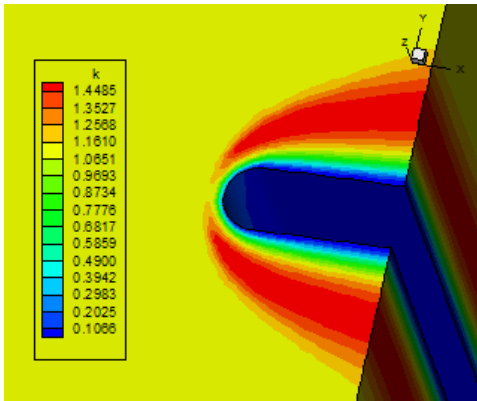
Figure 13: Turbulent kinetic energy contours (W88/MP)
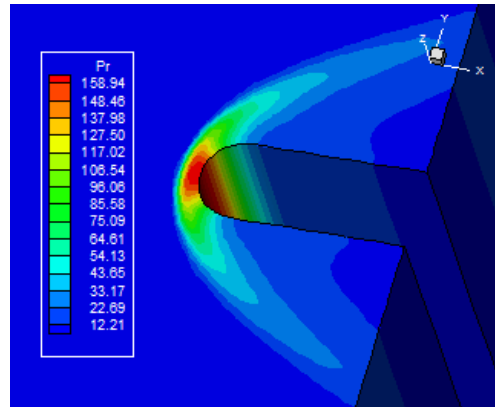
Figure 14: Pressure contours (W88/EM)
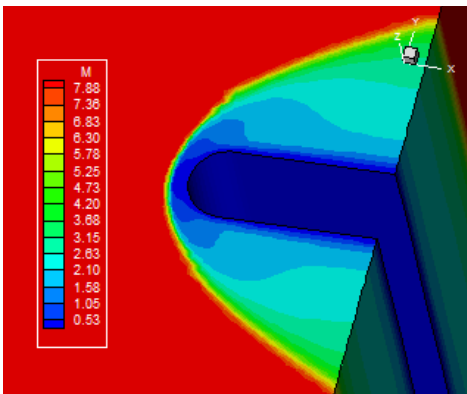
Figure 15: Mach number contours (W88/EM)
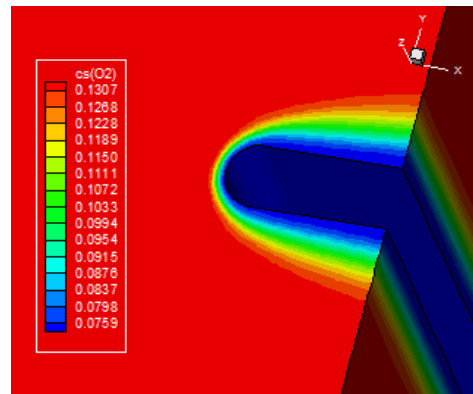
Figure 16: O_2 mass fraction contours (W88/EM)
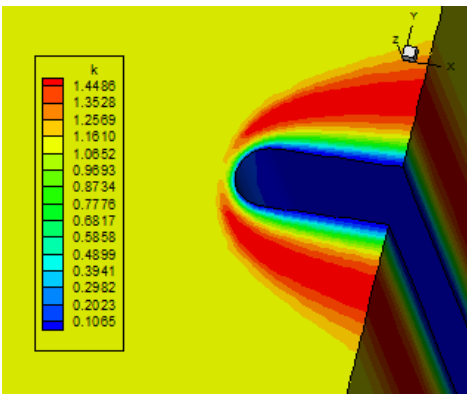
*Figure 17: Turbulent kinetic energy contours (W88/EM)*
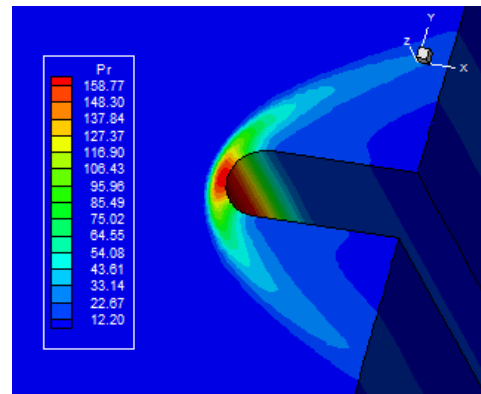
Figure 18: Pressure contours (YGO96/MP)
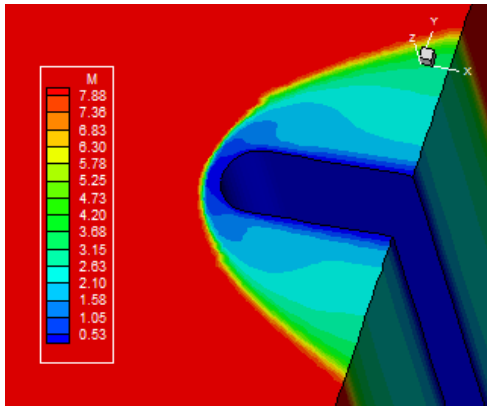
Figure 19: Mach number contours (YGO96/MP)   *Figure 20: O₂ mass fraction contours (YGO96/MP)*
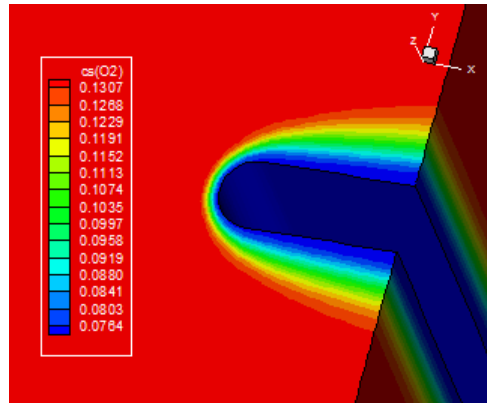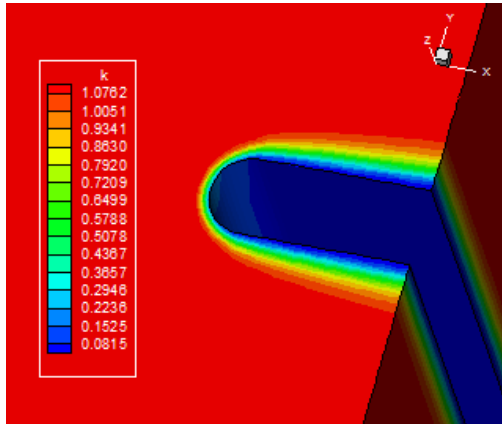
Figure 21: Turbulent kinetic energy contours (YGO96/MP)   *Figure 22. Pressure contours (YGO96/EM).*
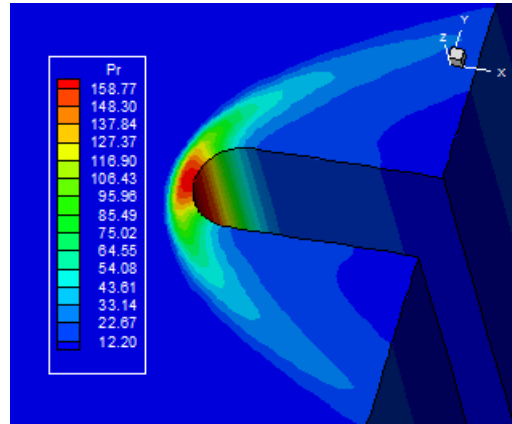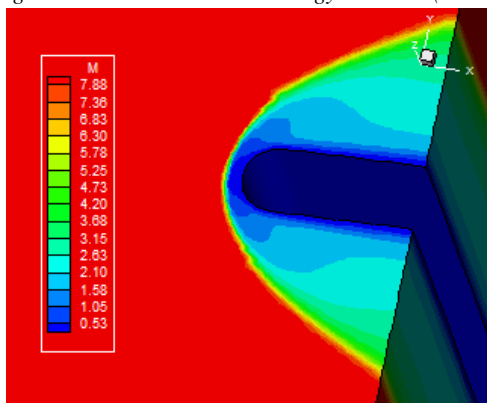
Figure 23: Mach number contours (YGO96/EM)   *Figure 24: O₂ mass fraction contours (YGO96/EM)*
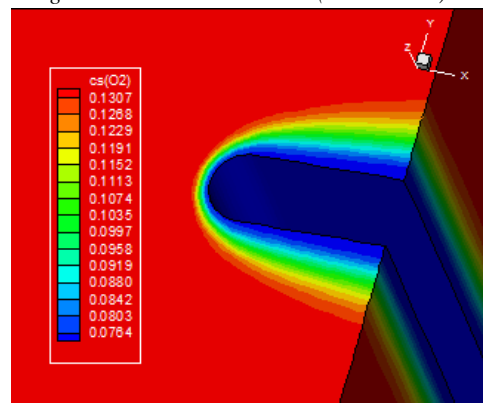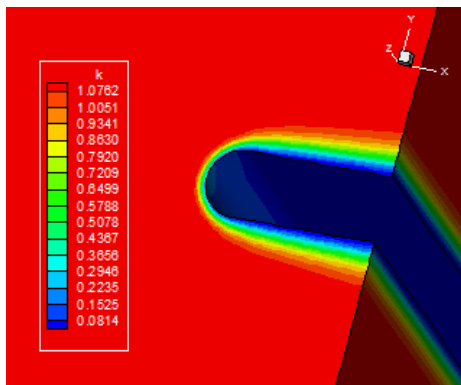
Figure 25: Turbulent kinetic energy contours (YGO96/EM)   *Figure 26: Pressure contours (C97/MP)*
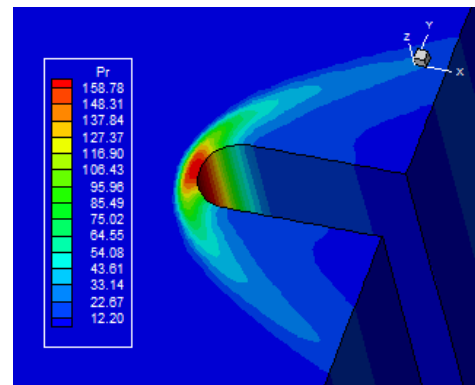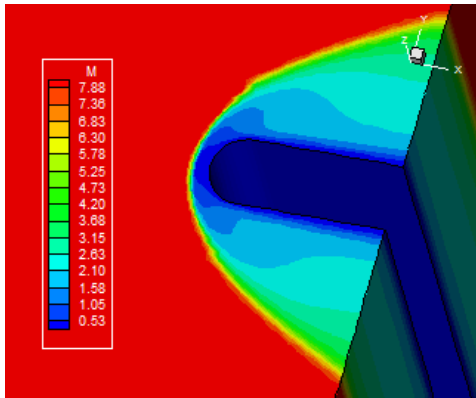
Figure 27: Mach number contours (C97/MP)
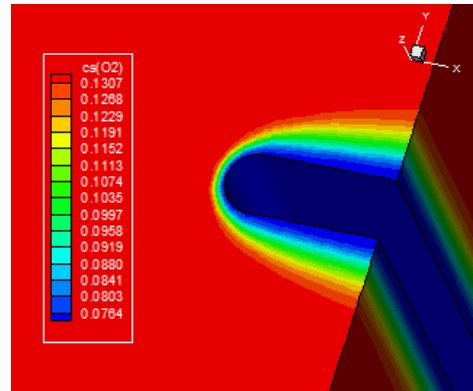
Figure 28: O₂ mass fraction contours (C97/MP)
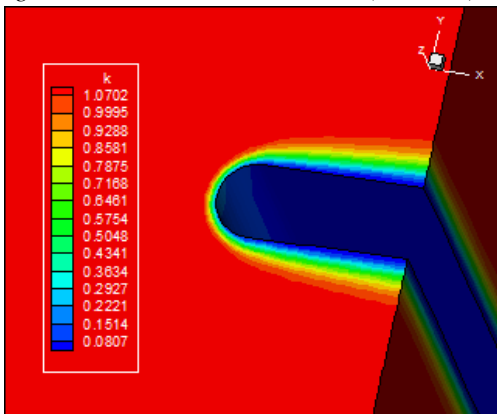
Figure 29: Turbulent kinetic energy contours (C97/MP)
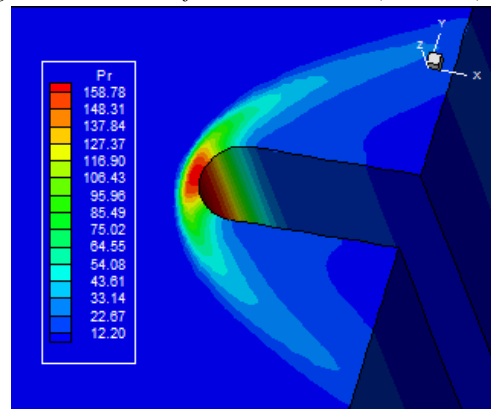
Figure 30: Pressure contours (C97/EM)
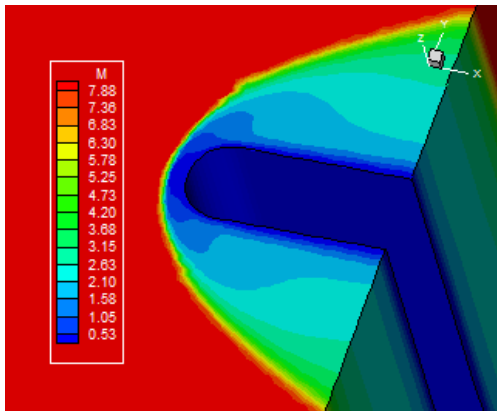
Figure 31: Mach number contours (C97/EM)
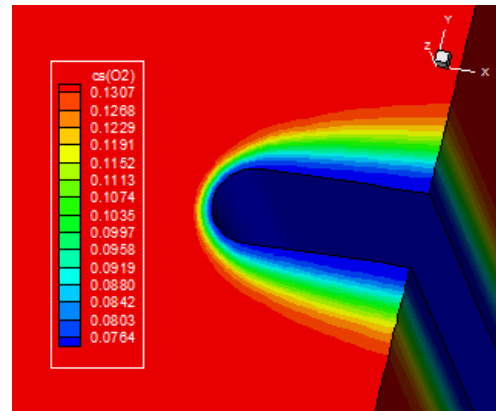
Figure 32: O₂ mass fraction contours (C97/EM)
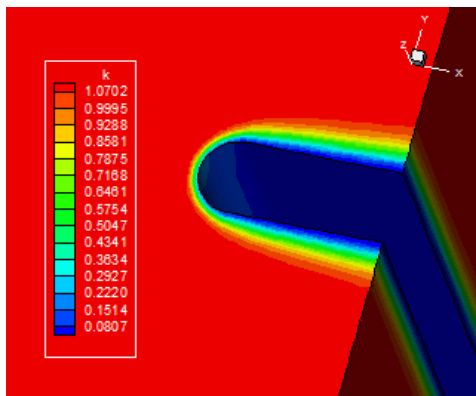
Figure 33: Turbulent kinetic energy contours (C97/EM)
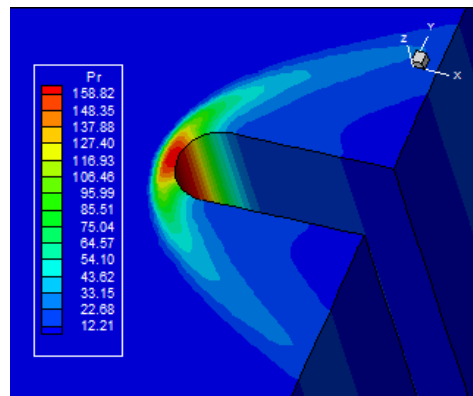

Figure 34: Pressure contours (RGYB98/MP)

Journal of Scientific and Engineering Research
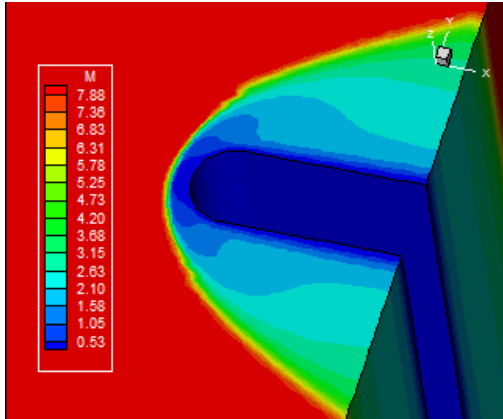
Figure 35: Mach number contours (RGYB98/MP)
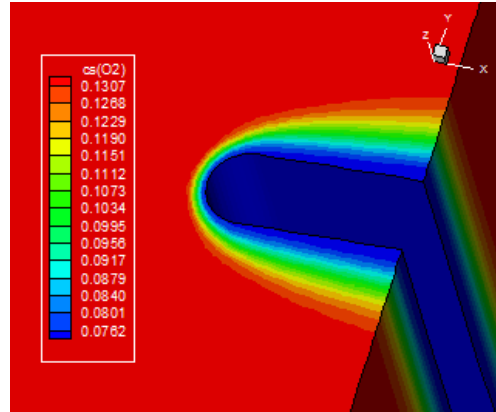
*Figure 36: O₂ mass fraction contours (RGYB98/MP)*
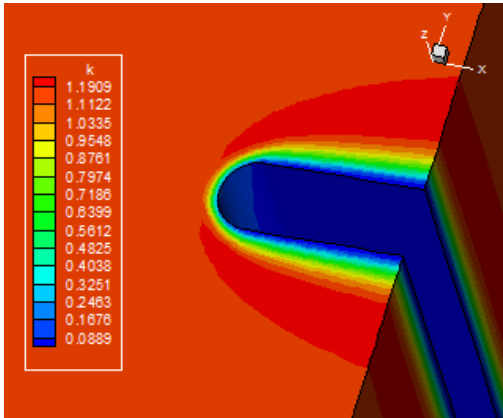
*Figure 37: Turbulent kinetic energy contours (RGYB98/MP)*
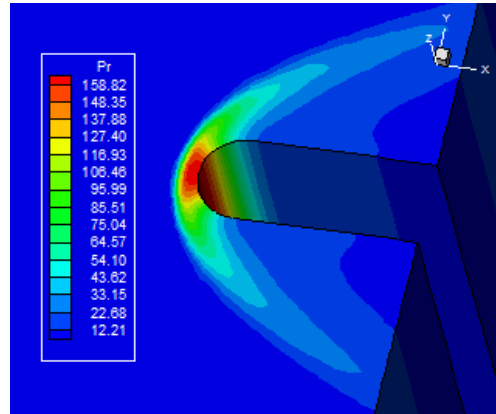
*Figure 38: Pressure contours (RGYB98/EM)*
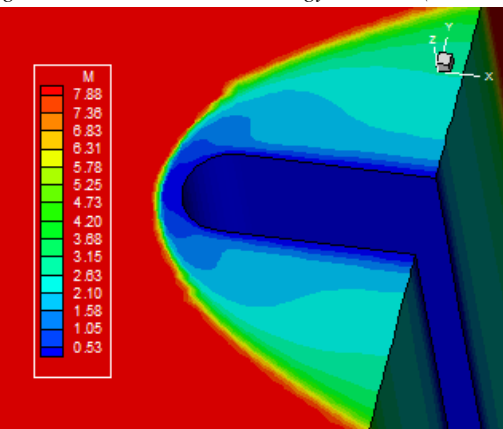
*Figure 39: Mach number contours (RGYB98/EM)*
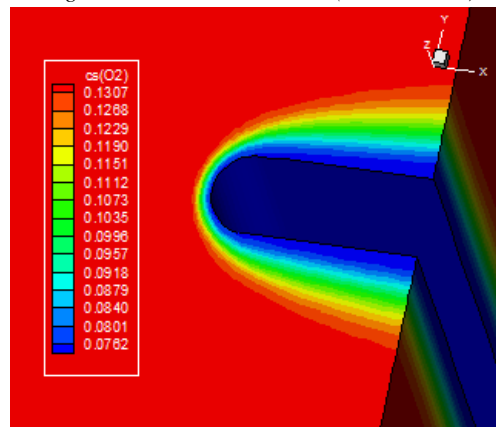
*Figure 40: O₂ mass fraction contours (RGYB98:EM)*
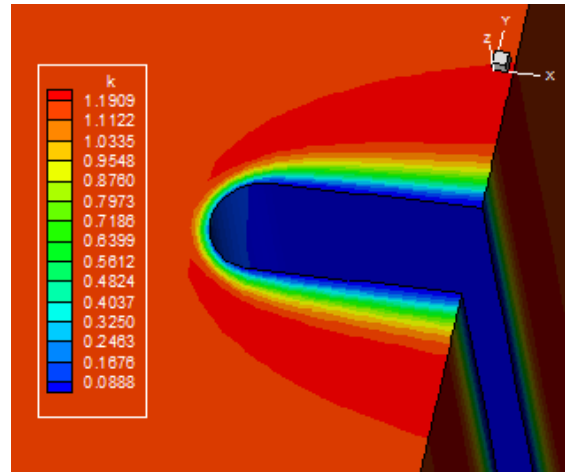
*Figure 41: Turbulent kinetic energy contours (RGYB98/EM)*
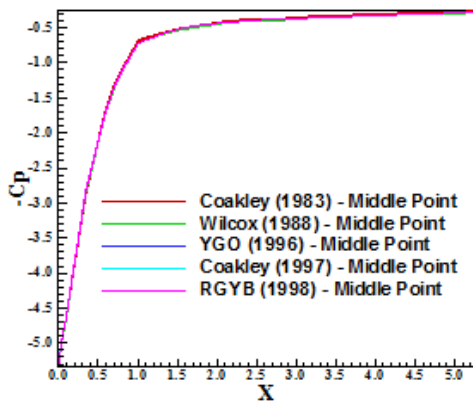
*Figure 42: Cp distributions (Middle Point).*
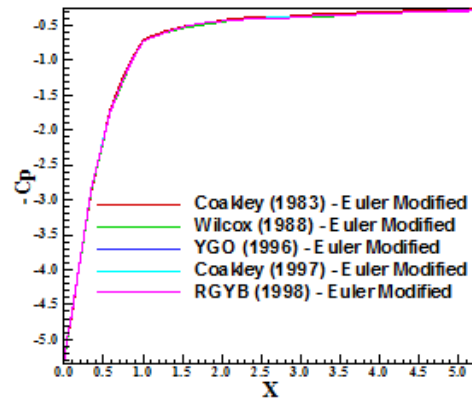
*Figure 43: Cp distributions (Euler Modified).*
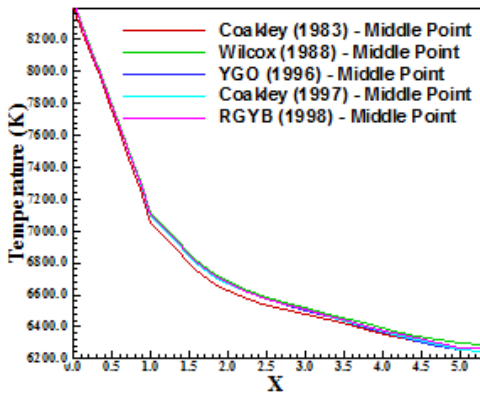
Figure 44: Wall temperature distributions (Middle Point)
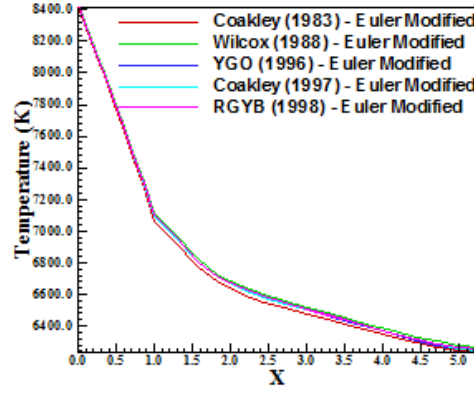
Figure 45: Wall temperature distributions (Euler Modified)

To calculate the stagnation pressure ahead of the blunt body, [29] presents in its B Appendix values of the normal shock wave properties ahead of the configuration. The ratio pr_0/pr_∞ is estimated as function of the normal Mach number and the stagnation pressure pr_0 can be determined from this parameter. Hence, to a freestream Mach number of 8.78, the ratio pr_0/pr_∞ assumes the value 99.98. The value of pr_∞ is determined by the following expression:

$$pr_\infty = \frac{pr_{initial}}{\rho_\infty \times a_\infty^2} \, . \tag{107}$$

In the present study, $pr_{initial} = 687N/m^2$, $\rho_\infty = 0.004kg/m^3$ and $a_\infty = 317.024m/s$. Considering these values, one concludes that $pr_\infty = 1.709$ (non-dimensional). Using the ratio obtained from [29], the stagnation pressure ahead of the configuration nose is estimated as 170.87 unities. Table 2 compares the values of the stagnation pressure obtained from the simulations with this theoretical value and shows the percentage errors. As can be seen, the best results are provided by the [4], turbulence model, when both the Middle Point and the Euler Modified have been employed, with an error of 6.95%. All solutions present an error inferior to 7.10%, which represents a good approximation to the theoretical value.

Table 2: Values of stagnation pressure and errors

Turbulence Model	Time Marching	pr_0	Error (%)
Coakley [4]	Middle Point	159.00	6.95
	Euler Modified	159.00	6.95
Wilcox [5]	Middle Point	158.93	6.99
	Euler Modified	158.94	6.98
YGO [6]	Middle Point	158.77	7.08
	Euler Modified	158.77	7.08
Coakley [7]	Middle Point	158.78	7.08
	Euler Modified	158.78	7.08
RGYB [8]	Middle Point	158.82	7.05
	Euler Modified	158.82	7.05

10.8. Computational Performance

Table 3 presents the computational data of the [10] scheme for the blunt body problem. It shows the CFL number and the number of iterations to convergence for all studied cases in the current work. It can be verified that the best performance is due to [10] when using the [4] turbulence model coupled with the Middle Point time marching method. It is important to note that the Middle Point time marching method is better than the Euler Modified time marching method in terms of number of iterations for convergence to all cases studied in this work.

Table 3: Computational data

Turbulence Model	Time Marching	CFL	Iterations
Coakley [4]	Middle Point	0.10	3,363
	Euler Modified	0.10	3,713
Wilcox [5]	Middle Point	0.10	3,671
	Euler Modified	0.10	3,935
YGO [6]	Middle Point	0.10	4,305
	Euler Modified	0.10	4,410
Coakley [7]	Middle Point	0.10	4,293
	Euler Modified	0.10	4,381
RGYB [8]	Middle Point	0.10	3,889
	Euler Modified	0.10	4,054

As final conclusion, it is possible to highlight the [4] turbulence model as the best performance in estimating the stagnation pressure ahead of the blunt body, in both time marching methods studied herein. Moreover, the [4] turbulence model coupled with a Middle Point method was the most efficient in terms of computational effort. It is also important to note that all turbulence models predicted the stagnation pressure value with errors inferior to 7.10%.

11. Conclusions

This work analyzed the Favre-averaged Navier-Stokes equations, using conservative and finite volume contexts, and employing structured spatial discretization. Turbulence is taken into account considering the

implementation of five k-ω two-equation turbulence models, based on the works of [4-8]. The numerical algorithm of [10] is used to perform the reentry flow numerical experiments, which give us an original contribution to the CFD community. TVD high resolution is obtained by the use of a MUSCL procedure. Two methods of time marching are evaluated to verify their potentialities, namely: Middle Point and Euler Modified. The "hot gas" hypersonic flow around a blunt body, in three-dimensions, is simulated. The convergence process is accelerated to steady state condition through a spatially variable time step procedure, which has proved effective gains in terms of computational acceleration ([11-12]). The reactive simulations involve Earth atmosphere chemical model of five species and seventeen reactions, based on the [13] model. N, O, N_2, O_2, and NO species are used to perform the numerical comparisons. The results have indicated that the [4] turbulence model yields the best prediction of the stagnation pressure value and is the most computationally efficient when using the Middle Point method.

As final conclusion, it is possible to highlight the [4] turbulence model as the best in the estimative of the stagnation pressure ahead of the blunt body, for both time integration methods studied herein. Moreover, the [4] turbulence model was the most efficient in terms of computational performance when using the Middle Point method. It is also important to note that all turbulence models predicted the stagnation pressure value with errors inferior to 7.10%, showing that excellent results can be obtained by an in-house developed CFD code.

Acknowledgments

References
[1]. J. R. Narayan, and S.S. Girimaji, "Turbulent Reacting Flow Computations Including Turbulence-Chemistry Interactions", *AIAA Paper 92-0342*, 1992.

[2]. P. A. Gnoffo, R. N. Gupta, and J. L. Shinn, "Conservation Equations and Physical Models for Hypersonic Flows in Thermal and Chemical Nonequilibrium", *NASA TP 2867*, 1989.

[3]. M. Liu, and M. Vinokur, "Upwind Algorithms for General Thermo-Chemical Nonequilibrium Flows", *AIAA Paper 89-0201*, 1989.

[4]. T. J. Coakley, "Turbulence Modeling Methods for the Compressible Navier-Stokes Equations", *AIAA Paper 83-1693*, 1983.

[5]. D. C. Wilcox, "Reassessment of the Scale-Determining Equation for Advanced Turbulence Models", *AIAA Journal*, vol. 26, No. 11, 1988, pp. 1299-1310.

[6]. D. A. Yoder, N. J. Georgiadids, and P. D. Orkwis, "Implementation of a Two-Equation K-Omega Turbulence Model in NPARC", *AIAA Paper 96-0383*, 1996.

[7]. T. J. Coakley, "Development of Turbulence Models for Aerodynamic Applications", *AIAA Paper 97-2009*, 1997.

[8]. C. L. Rumsey, T. B. Gatski, S. X. Ying, and A. Bertelrud, "Prediction of High-Lift Flows Using Turbulent Closure Models", *AIAA Journal*, vol. 36, No. 5, 1998, pp. 765-774.

[9]. C. Hirsch, *Numerical Computation of Internal and External Flows – Computational Methods for Inviscid and Viscous Flows*, John Wiley & Sons Ltd, 691p, 1990.

[10]. B. Van Leer, "Flux-Vector Splitting for the Euler Equations", *Lecture Notes in Physics*, Springer Verlag, Berlin, vol. 170, 1982, pp. 507-512.

[11]. E. S. G. Maciel, *Simulations in 2D and 3D Applying Unstructured Algorithms, Euler and Navier-Stokes Equations – Perfect Gas Formulation*, Saarbrücken, Deutschland: Lambert Academic Publishing (LAP), 2015, Ch. 1, pp. 26-47.

[12]. E. S. G. Maciel, *Simulations in 2D and 3D Applying Unstructured Algorithms, Euler and Navier-Stokes Equations – Perfect Gas Formulation*, Saarbrücken, Deutschland: Lambert Academic Publishing (LAP), 2015, Ch. 6, pp. 160-181.

[13]. S. K. Saxena and M. T. Nair, "An Improved Roe Scheme for Real Gas Flow", *AIAA Paper 2005-587*, 2005.

[14]. J. R. Narayan, "Computation of Compressible Reacting Flows Using a Two-Equation Turbulence Model", *4th International Symposium on Computational Fluid Dynamics*, Davis, California, September, 1991.

[15]. F. A. Williams, *Combustion Theory*, Addison-Wesley Publishing Company, Inc., Reading, MA, pp. 358-429, 1965.

[16]. J. P. Drummond, M. H. Carpenter, and D. W. Riggins, "Mixing and Mixing Enhancement in Supersonic Reacting Flows", *High Speed Propulsion Systems: Contributions to Thermodynamic Analysis*, ed. E. T. Curran and S. N. B. Murthy, American Institute of Astronautics and Aeronautics (AIAA), Washington, D. C., 1990.

[17]. E. S. G. Maciel, and A. P. Pimenta, "Chemical Non-Equilibrium Reentry Flows in Two-Dimensions – Part I", *WSEAS Transactions on Fluid Mechanics*, vol. 8, Issue 1, 2013, pp. 1-20.

[18]. E. S. G. Maciel, and A. P. Pimenta, "Chemical Non-Equilibrium Reentry Flows in Two-Dimensions – Part II", *WSEAS Transactions on Fluid Mechanics*, vol. 8, Issue 2, 2013, pp. 50-79.

[19]. A. Favre, *Statistical Equations of Turbulent Gases*, Institut de MechaniqueStatistique de la Turbulence, Marseille.

[20]. E. S. G. Maciel, "Turbulent Thermochemical Non-Equilibrium Reentry Flows in 2D", *Computational and Applied Mathematics Journal*, vol. 1, Issue 4, 2015, pp. 201-224.

[21]. R. K. Prabhu, "An Implementation of a Chemical and Thermal Nonequilibrium Flow Solver on Unstructured Meshes and Application to Blunt Bodies", *NASA CR-194967*, 1994.

[22]. D. Ait-Ali-Yahia, and W. G. Habashi, "Finite Element Adaptive Method for Hypersonic Thermochemical Nonequilibrium Flows", *AIAA Journal*, vol. 35, No. 8, 1997, 1294-1302.

[23]. R. Radespiel, and N. Kroll, "Accurate Flux Vector Splitting for Shocks and Shear Layers", *Journal of Computational Physics*, vol. 121, 1995, pp. 66-78.

[24]. L. N. Long, M. M. S. Khan, and H. T. Sharp, "Massively Parallel Three-Dimensional Euler / Navier-Stokes Method", *AIAA Journal*, vol. 29, No. 5, 1991, pp. 657-666.

[25]. B. Van Leer, Towards the Ultimate Conservative Difference Scheme. II. Monotonicity and Conservation Combined in a Second-Order Scheme, *Journal of Computational Physics*, vol. 14, 1974, pp. 361-370.

[26]. P. L. Roe, In *Proceedings of the AMS-SIAM Summer Seminar on Large-Scale Computation in Fluid Mechanics*, Edited by B. E. Engquist et al, *Lectures in Applied Mathematics,*vol. 22, 1983, p. 163.

[27]. R. W. Fox, and A. T. McDonald, *Introdução à Mecânica dos Fluidos*, Guanabara Editor, 1988.

[28]. E. S. G. Maciel, "Simulação Numérica de Escoamentos Supersônicos e HipersônicosUtilizando Técnicas de Dinâmica dos Fluidos Computacional", *Doctoral Thesis*, ITA, CTA,   São José dos Campos, SP, Brazil, 2002.

[29]. J. D. Anderson Jr., *Fundamentals of Aerodynamics*, McGraw-Hill, Inc., 5th Edition, 1008p., 2010.